Thin-Walled Structures 189 (2023) 110857

Contents lists available at ScienceDirect

Thin-Walled Structures

journal homepage: www.elsevier.com/locate/tws

Full length article

Optimisation and testing of wire arc additively manufactured steel stub columns

Xin Meng [a,*], Ben Weber [a], Masashi Nitawaki [b], Leroy Gardner [a]

[a] Department of Civil and Environmental Engineering, Imperial College London, London, UK
[b] Shimizu Corporation, Japan

ARTICLE INFO

Keywords:
Additive manufacturing
Digital image correlation
3D laser-scanning
Structural optimisation
Testing
Wire arc additive manufacturing (WAAM)

ABSTRACT

Wire arc additive manufacturing (WAAM), a method of directed energy deposition (DED) for metal 3D printing, is capable of producing intricate parts at a relatively high rate and low cost. Despite the great potential of WAAM for applications in construction, knowledge of the performance of WAAM structural elements is still lacking, and the geometric freedom is yet to be fully harnessed. This study is therefore aimed at investigating the local buckling behaviour of carbon steel WAAM elements and exploring the opportunity for improved structural efficiency through optimisation. An optimisation study was initially conducted to derive optimal stiffener layouts for square hollow sections (SHS) under compression. A total of six plain SHS with a broad range of width-to-thickness ratios, along with two SHS strengthened with optimised stiffeners, were manufactured via WAAM and tested. The six benchmark WAAM SHS profiles were examined to allow direct comparisons with conventionally-produced SHS. 3D laser-scanning was carried out to capture the geometric features of the WAAM specimens, and digital image correlation (DIC) was adopted for the full-field measurement of their structural responses during testing. The WAAM SHS stub columns were shown to have comparable load-carrying capacities to conventionally-produced SHS in the stocky range, but exhibited inferior local buckling behaviour in the slender range. Comparisons with the Eurocode 3 (EC3) resistance predictions showed that the existing Class 3 slenderness limit and effective width method specified in EC3 for plated structures may be overly optimistic for WAAM steel elements owing to their typically larger geometric imperfections. Finally, the SHS strengthened with optimised stiffeners were shown to exhibit significantly improved structural efficiency over both the WAAM and conventionally-manufactured plain SHS, bringing disproportionate increases in load-carrying and deformation capacity relative to the increases in mass.

1. Introduction

Metal additive manufacturing (AM), also known as metal 3D printing, is the process of making metal parts from 3D digital model data, usually by the deposition of melted metal powder or wire layer upon layer [1–3]. Metal AM allows intricate parts to be made without the design constraints of traditional formative or subtractive manufacturing, reduces lead times for on-demand manufacturing, and enables highly automated and decentralised production [2,4]. Metal AM is becoming widely used in the medical, automotive and aerospace industries, and is now also receiving increasing attention from the construction sector.

To date, directed energy deposition (DED) and powder bed fusion (PBF) are the most widely used techniques for metal AM [5]. Other techniques feasible for metal AM include binder jetting (BJT) and sheet lamination (SHL), although the technology is still under development and is less commercially accessible [5]. Wire arc additive manufacturing (WAAM) is a method of DED that uses an electric arc as a fusion source to melt metal wire feedstock [4]. Owing to the relatively high deposition rate (typically around 1.5 kg/h), large build volume and low costs, WAAM is widely recognised to be the most suitable technique for construction applications. Several pilot projects employing WAAM have been successfully deployed in construction. A prominent example is the MX3D bridge in the Netherlands, the first metal 3D printed bridge in the world, shown in Fig. 1 [6].

The material and structural behaviour of WAAM elements differ from those of conventionally-produced elements to an extent that depends on the printing process, process parameters, part geometry, printing quality and control and so on [3]. There has been a growing body of research devoted to investigating the mechanical properties of WAAM stainless steel [7–12], carbon steel [12–16], aluminium alloy [17–19] and titanium alloy [20–22], but relatively few studies have been devoted to understanding the structural performance of WAAM elements [23–27], and overall, relevant experimental data are lacking. To bridge this knowledge gap and establish efficient and reliable design guidance for WAAM structures, further investigation into the structural

* Corresponding author.
E-mail address: xin.meng15@imperial.ac.uk (X. Meng).

https://doi.org/10.1016/j.tws.2023.110857
Received 14 March 2023; Received in revised form 10 May 2023; Accepted 12 May 2023
Available online 3 July 2023
0263-8231/© 2023 The Author(s). Published by Elsevier Ltd. This is an open access article under the CC BY license (http://creativecommons.org/licenses/by/4.0/).



Fig. 1. MX3D bridge in Amsterdam, the Netherlands [6].
Source: Photographer: Adriaan de Groot, credit: MX3D.

behaviour of WAAM elements is needed; this is the main focus of the present study.

The geometric freedom granted by metal AM naturally creates opportunities for structural optimisation, the practical application of which has long been restricted by manufacturability using conventional formative and subtractive methods. The viability of WAAM, in terms of both costs and environmental impact, hinges upon a number of factors including the achievable material savings and deposition rates; it is therefore crucial to use WAAM strategically. A number of optimisation studies on metal AM structural elements and systems has been carried out [28–31], although countless possibilities are yet to be explored.

The primarily objective of this study is to investigate the local buckling behaviour of WAAM carbon steel structural elements subjected to axial compression, while also exploring the opportunity to improve the structural efficiency of compression members through structural optimisation. A series of stub column specimens was manufactured via WAAM using high strength steel wire as the feedstock material. Standard square hollow sections (SHS) were examined to enable direct comparisons with conventionally-produced SHS, thereby isolating the influence of the unique geometric and material features inherent to WAAM. A shape optimisation study was performed based on elastic buckling stresses to derive the optimal configurations of stiffeners for SHS; two selected designs of the strengthened SHS were printed and tested. In total, eight WAAM stub column specimens were tested in this experimental programme. The undulating surface geometries of the WAAM test specimens were captured using the 3D laser-scanning technique, and full-field measurements of the test responses were realised by means of digital image correlation (DIC). The obtained WAAM stub column test data were compared with existing test data on conventionally-formed SHS, and the suitability of the existing Eurocode 3 (EC3) structural design rules for WAAM SHS stub columns was finally assessed.

2. Optimisation of strengthened SHS

2.1. General

Stiffeners are widely used in metallic structures to enhance the local buckling resistance, but are rarely seen in tubular members because the structural benefits are often outweighed by the difficulty of fabrication. This is no longer a limitation with the novel metal AM technology.

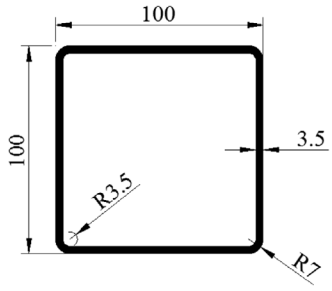


Fig. 2. Benchmark SHS profile (dimensions in mm).

In this section, an optimisation study was conducted to determine the optimal configurations of stiffeners for square hollow sections (SHS) under axial compression.

2.2. Methodology

Existing studies into shape optimisation of structural profiles have been predominantly focussed on cold-formed open sections [32–36], which can be fabricated with relative ease. However, there is limited research into the optimisation of stiffened structural hollow sections due to manufacturability. Only a few experimental studies on stiffened hollow sections fabricated by welding stiffeners to plates or C sections have been conducted [37–39].

In the present investigation, shape optimisation of stiffened SHS produced using WAAM was carried out. A typical SHS profile — 100×100×3.5 (height × width × thickness, in mm), as shown in Fig. 2, was adopted for the optimisation. A selection of stiffener layouts was initially set out based on structural engineering principles, as shown in Fig. 3, which can be broadly categorised into two types: (a) intermediate plate stiffeners and (b) corner stiffeners. Note that the scope of the present study was limited to longitudinal stiffeners and constant cross-section profiles.

The location and dimensions of the stiffeners were taken as the design variables. To quantify the structural efficiency of the stiffened SHS relative to the corresponding plain (i.e. unstiffened) SHS, a normalised efficiency parameter μ was introduced based on the elastic buckling stress of the cross-section, as given by Eq. (1), where σ_{cr} is

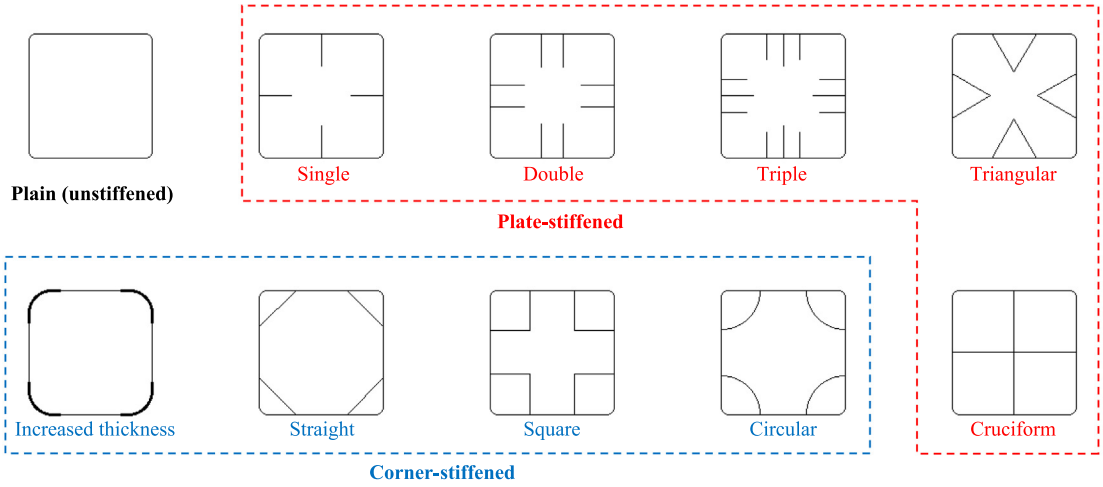


Fig. 3. Various stiffener layouts for SHS.

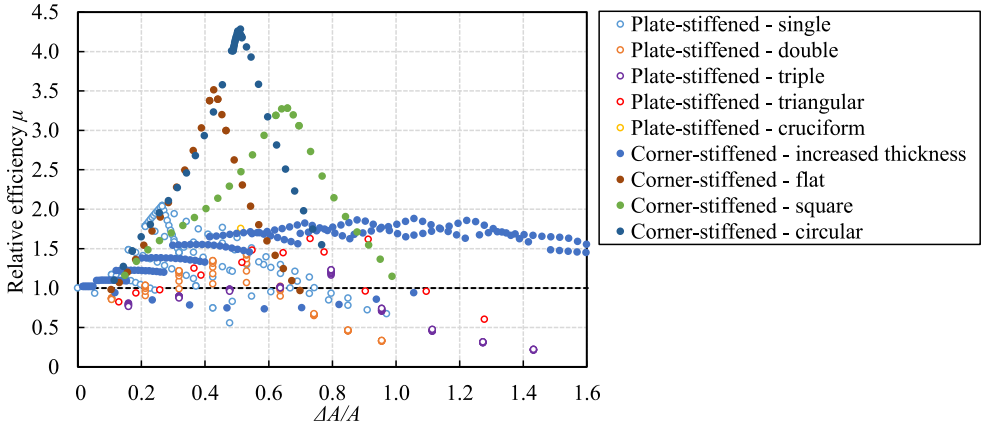


Fig. 4. Normalised efficiency of SHS with different stiffener layouts.

the elastic critical buckling stress of the stiffened SHS, and $\sigma_{cr,eq}$ is the elastic critical buckling stress of the equivalent plain SHS with the same outer profile and cross-sectional area but increased wall thickness. The elastic buckling stresses were calculated based on the centreline geometry using the finite strip analysis software CUFSM [40].

$$\mu = \frac{\sigma_{cr}}{\sigma_{cr,eq}} \tag{1}$$

The objective of the optimisation was to maximise the normalised efficiency μ for a given increase in cross-sectional area ΔA. The minimum thickness was set to 3.5 mm according to the constraints of the utilised WAAM process. Owing to the relatively low computational costs, a parametric study was performed to determine the optimal stiffener layouts.

2.3. Results and discussion

The obtained normalised efficiency parameters μ associated with different stiffener layouts are plotted against the normalised increase in cross-sectional area (denoted by $\Delta A/A$, where A is the cross-sectional area of the benchmark plain SHS shown in Fig. 2 and ΔA is the increase in cross-sectional area of the stiffened SHS relative to the benchmark) in Fig. 4. Overall, the examined stiffener layouts led to an increased efficiency when suitably proportioned, and the corner stiffeners were shown to be more efficient in general compared with the intermediate plate stiffeners for the benchmark SHS. Among the considered plate stiffener layouts, the single plate stiffeners led to the highest normalised efficiency $\mu = 2.04$ at a relative cross-sectional area increase of 26.5%, while the circular corner stiffener provided the highest overall relative efficiency $\mu = 4.24$ at $\Delta A/A = 50.2\%$; the corresponding optimal stiffened SHS profiles are shown in Fig. 5. The signature curves obtained from CUFSM [40], which describe the relationship between the critical buckling stress and the buckling half-wavelength, are shown in Fig. 6. The critical cross-sectional buckling modes are also plotted on the signature curves, where the yellow and red profiles represent the original and the buckled shapes respectively. The optimal layouts shown in Fig. 5 were selected to be printed and tested in the subsequent experimental programme.

3. Specimen manufacture

A total of six plain SHS stub columns with varying plate width-to-thickness ratios, plus two optimised stiffened SHS shown in Fig. 5, were manufactured by the Dutch company MX3D using their proprietary multiaxis robotic WAAM technology [41]. A 6-axis robotic arm and a metal inert gas (MIG) welding machine were employed for printing. Grade ER110S-G welding wires with a diameter of 1.2 mm were adopted as the feedstock. The chemical composition and mechanical properties provided in the wire certificate is displayed in Tables 1 and 2 respectively. The welding wires were continuously fed, melted and deposited onto a 1000×1000×25 mm substrate plate to build up the

Table 1
Chemical composition of welding wire specified in manufacturer certificate (in weight percentage).

C	Si	Mn	P	S	Cu	Al	Cr	Mo	Ni	V
0.09	0.55	1.55	0.007	0.014	0.061	0.003	0.25	0.22	1.42	0.084
Ti	Nb	Co	Pb	Sn	B	As	Zr	Ta	Sb	Ca
0.001	0.001	0.016	0.001	0.006	0.0001	0.001	0.001	0.001	0.001	0.0002

Table 2
Mechanical properties of weld metal specified in manufacturer certificate.

	f_y (N/mm^2)	f_u (N/mm^2)	ε_f (%)	Impact energy
Minimum guaranteed value	690	770	17	47 J @ −40 °C
Test result	735	799	18	55 J @ −40 °C

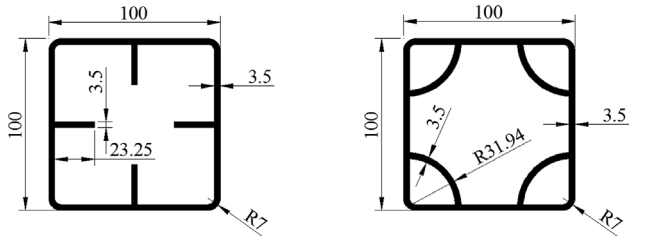
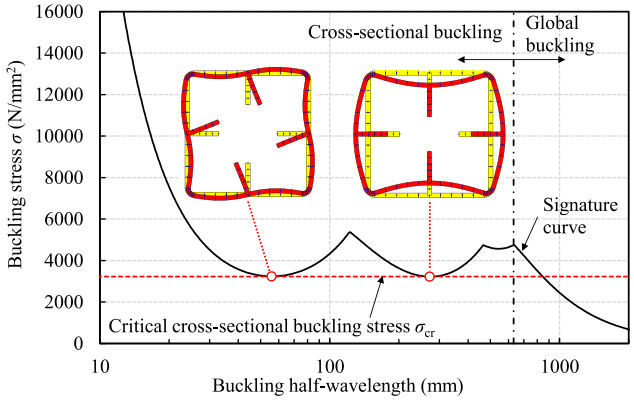
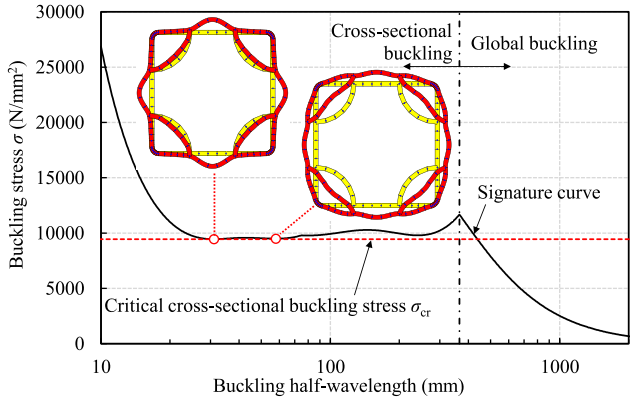


Fig. 5. Optimal stiffened SHS profiles (dimensions in mm): plated-stiffened (left) and corner-stiffened (right).



(a) Optimal single plate-stiffened SHS



(b) Optimal circular corner-stiffened SHS

Fig. 6. Signature curves and critical cross-sectional buckling modes of optimal stiffened SHS profiles: (a) plate-stiffened and (b) corner-stiffened.

Table 3
Key process parameters for manufacture of stub column specimens.

Process parameter	Nominal thickness t	
	3.5 mm	8 mm
Toolpath	Single pass	Double pass
Current (A)	106	152
Voltage (V)	15.2	16.4
Wire feeding speed (m/min)	2.3	3.5
Travel speed (mm/s)	11	9.5
Interpass temperature (°C)	250	250
Stick out (mm)	9–12	9–12
Wire grade	ER110S-G	ER110S-G
Wire diameter (mm)	1.2	1.2
Shield gas type	M12 ARCAL Chrome	M12 ARCAL Chrome
Shield gas composition	98% Ar + 2% CO_2	98% Ar + 2% CO_2
Gas flow (L/min)	22	22
Cooling method	Passive cooling	Passive cooling
Average layer height (mm)	1	1.5
Average layer width (mm)	3.7	8.4

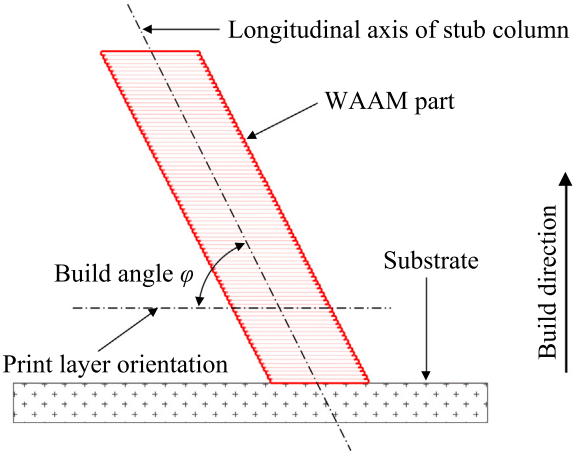


Fig. 7. Definitions of build angle and build direction.

specimen in a layer-by-layer manner. The stub column specimens had two different nominal thickness – 3.5 mm and 8 mm. The nominally 3.5 mm-thick specimens were printed with a single pass, while the 8 mm-thick specimens were printed with double passes. The manufacturing parameters for the two different wall thicknesses are summarised in Table 3. The build angle φ is defined as the angle between the longitudinal axis of the stub column specimen and the print layer orientation, as illustrated in Fig. 7. All stub column specimens were manufactured with a build angle of 90°, except one with a build angle of 45° to investigate the influence of the loading direction relative to print layer orientation.

The toolpaths adopted for the two SHS strengthened with optimised stiffeners are illustrated in Fig. 8. For the plate-stiffened design, the SHS profile was initially printed with the start point randomised and the deposition directions alternated between layers. The stiffeners were

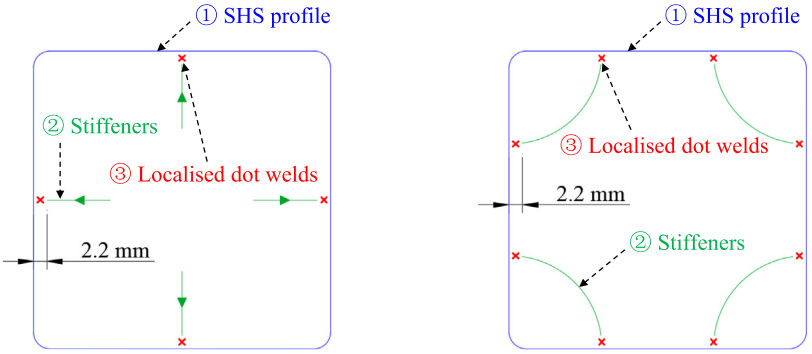


Fig. 8. Toolpaths (not to scale) for plated-stiffened SHS (left) and corner-stiffened SHS (right).

Table 4
Measured geometric properties of WAAM stub column specimens.

Specimen ID	Cross-section (mm)	Toolpath	φ (°)	H (mm)	B (mm)	R (mm)	r (mm)	t (mm)	L (mm)	A_{scan} (mm^2)	$A_{density}$ (mm^2)	$A_{scan}/A_{density}$
P1	58×58×8	Double pass	90	57.13	57.63	10.2	7.7	8.27	151.68	1630.3	1598.4	1.020
P2	53.5×53.5×3.5	Single pass	90	52.88	52.85	6.0	6.5	3.61	152.47	714.0	693.0	1.030
P3	103.5×103.5×3.5	Single pass	90	102.77	102.34	7.3	7.2	3.63	302.14	1429.6	1381.1	1.035
P4	103.5×103.5×3.5	Single pass	45	102.25	104.12	6.7	7.2	3.67	301.78	1484.0	1448.1	1.025
P5	158×158×8	Double pass	90	156.97	156.87	10.4	8.8	8.07	452.56	4808.1	4750.2	1.012
P6	203.5×203.5×3.5	Single pass	90	201.52	202.37	7.5	6.8	3.62	603.13	2869.8	2801.0	1.025
S1	100×100×3.5 (plate stiffened)	Single pass	90	99.50	99.50	12.3	10.3	3.34	301.94	1677.67	1628.6	1.030
S2	100×100×3.5 (corner stiffened)	Single pass	90	99.32	99.68	12.8	9.6	3.51	302.06	2008.4	1981.9	1.013

subsequently deposited following the directions shown in Fig. 8. The corner-stiffened SHS was printed in the same manner, except that the deposition direction for the curved stiffeners was also alternated between layers. The intersection between the SHS and stiffeners, which is a typical crossing feature that commonly poses a challenge to the WAAM process, is prone to non-uniform layer heights and printing defects when directly crossing toolpaths are employed [42]. A number of studies has been devoted to improving the path planning strategies for such crossing features [43–45]. In the present study, a 2.2 mm gap was left between the toolpaths for the SHS and stiffeners, which was eventually closed with a localised dot weld, to minimise the non-uniformity of layer heights. Upon completion of printing, the stub column specimens were extracted from their substrates using a plasma arc cutter.

4. Geometric analysis

4.1. General

A total of eight WAAM SHS stub column specimens (six plain and two stiffened) was manufactured and examined in this study. The nominal cross-section profiles, along with the corresponding toolpaths and build angles, are summarised in Table 4. The test specimens were labelled as P1–P6 and S1–S2, where P and S stand for plain and stiffened SHS respectively.

Prior to compressive testing, 3D laser-scanning of the WAAM stub column specimens was carried out to investigate their unique geometric characteristics. Their mean cross-sectional dimensions were initially obtained, and statistical analyses were subsequently conducted to evaluate the variability of the key dimensional parameters. Local geometric imperfections, which can influence the local buckling response and ultimate load-carrying capacity of the stub column specimens, were also examined using the scanned data.

4.2. Specimen preparation

The as-printed WAAM stub column specimens were firstly cut using a band saw to a length equal to three times the larger cross-sectional dimensions, which was deemed long enough to include a representative pattern of local geometric imperfections and residual stresses, but short enough to preclude global buckling effects [46]. The specimen surfaces were grit blasted using glass beads, which has been shown to be abrasive enough for surface cleaning while remaining sufficiently fine not to affect their geometry [7,23]. The ends of the specimens were then lapped flat and square to ensure a uniform distribution of compressive stresses. The test specimens after preparation are displayed in Fig. 9.

4.3. Laser-scanning

To accurately capture the undulating surface geometry inherent to the WAAM process, 3D laser-scanning was performed for all stub column specimens using a FARO ScanArm. Full scans of the outer surfaces were obtained for all the test specimens; for the inner surfaces, only the accessible regions near the ends were captured. The obtained point cloud data were initially processed in Geomagic Wrap [47] and then imported into Matlab [48] and Rhino [49] for post-processing and analysis. The raw point clouds were gridded with a spacing of 0.2 mm, leading to at least five points across each print layer, which was considered to be fine enough for capturing the surface undulations at reasonable computational costs.

4.4. Geometric properties

The cross-section height H, breadth B, thickness t and area A, as well as the member length L, of the examined WAAM SHS specimens were obtained by analysing contours of the scans at 0.2 mm intervals along the longitudinal direction, as illustrated in Fig. 10. The outer and inner corner radii of the SHS profiles, denoted by R and r respectively, were derived by fitting a cylinder to the scanned data within the corner region — see Fig. 11. A summary of the mean geometric properties is provided in Table 4.

The mean cross-sectional areas were also calculated based on the weight and density of the test specimens, as given by Eq. (2), where W is the self-weight of the specimens measured using a high-precision balance and ρ is the density of the examined WAAM materials, as

Table 5
Statistical parameters for geometric properties of WAAM stub column specimens.

Specimen ID	Cross-section	Toolpath	φ (°)	s_H (mm)	s_B (mm)	s_t (mm)	s_A (mm^2)	V_H	V_B	V_t	V_A
P1	58×58×8	Double pass	90	0.25	0.19	0.20	19.2	0.004	0.003	0.025	0.012
P2	53.5×53.5×3.5	Single pass	90	0.08	0.08	0.11	8.2	0.002	0.002	0.032	0.012
P3	103.5×103.5×3.5	Single pass	90	0.11	0.10	0.16	15.6	0.001	0.001	0.043	0.011
P4	103.5×103.5×3.5	Single pass	45	0.08	0.79	0.22	22.2	0.001	0.008	0.059	0.015
P5	158×158×8	Double pass	90	0.18	0.21	0.23	76.8	0.001	0.001	0.028	0.016
P6	203.5×203.5×3.5	Single pass	90	4.62	4.59	0.16	68.5	0.023	0.023	0.045	0.024
S1	100×100×3.5 (plate stiffened)	Single pass	90	0.22	0.25	0.11	48.1	0.002	0.003	0.033	0.029
S2	100×100×3.5 (corner stiffened)	Single pass	90	0.13	0.14	0.33	128.7	0.001	0.001	0.093	0.064

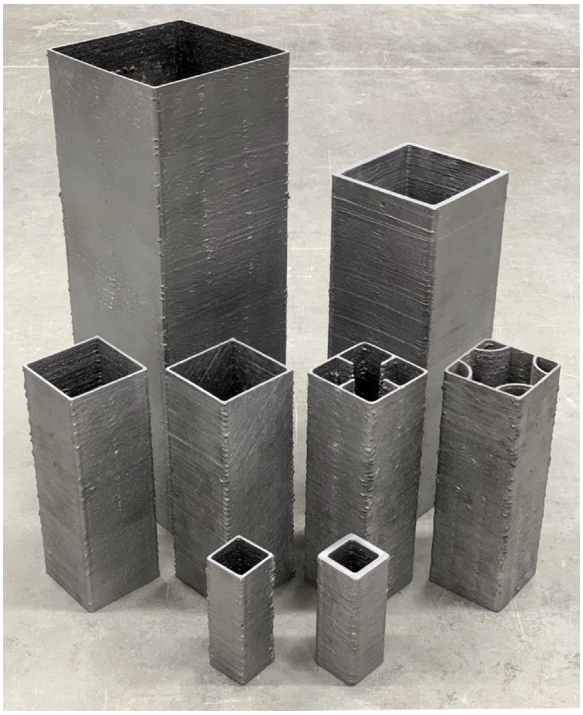


Fig. 9. WAAM stub column specimens after preparation.

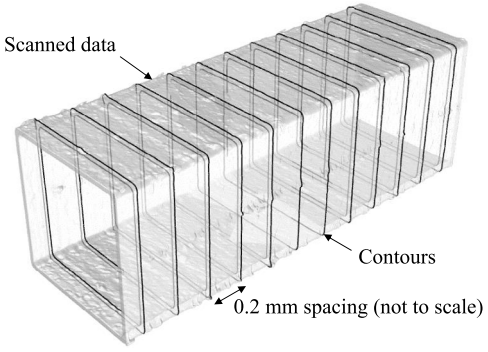


Fig. 10. Analysis of contours extracted from scanned data.

measured and reported in [16]. In general, there were slight differences (below 3.5%) between the cross-sectional areas derived based on the scanned data (denoted by A_{scan}) and the density (denoted by A_{density}), which can be attributed to the incomplete inner scans used in the analysis of cross-sectional areas and the measurement error of the laser scanner. Thus, the cross-sectional area obtained based on the weight

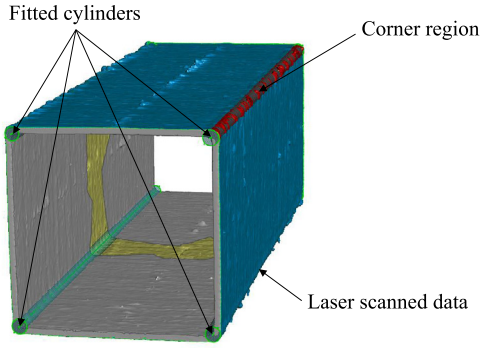


Fig. 11. Determination of corner radii based on scanned data.

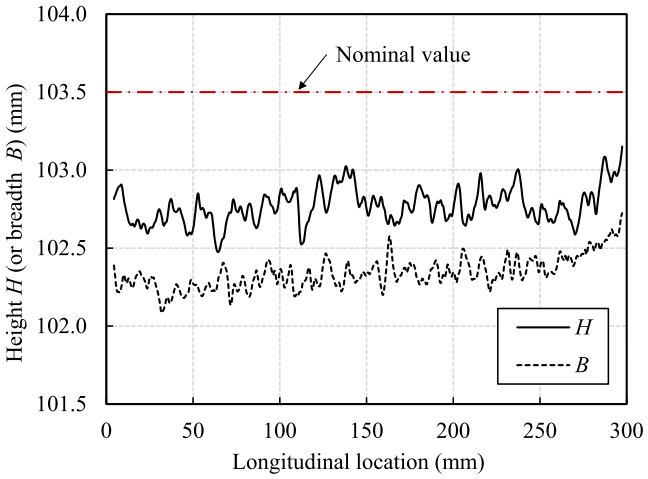
and density A_{density} was deemed more appropriate.

$$A_{\text{density}} = \frac{W}{\rho L} \tag{2}$$

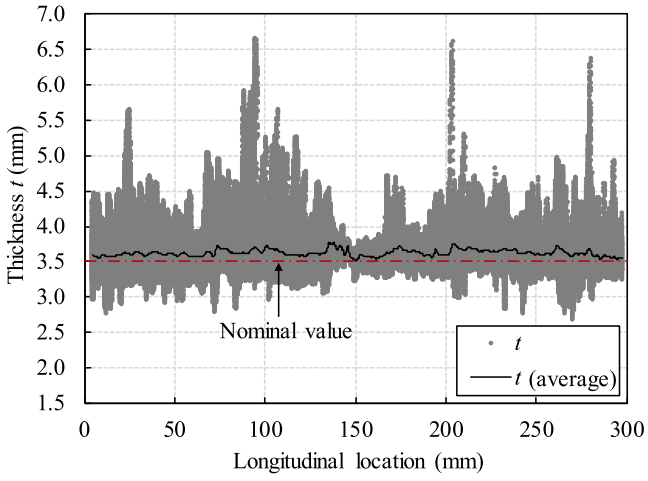
Typical distributions of the dimensional parameters and the corresponding histograms are shown in Fig. 12 and Fig. 13 respectively. The values of the thickness t at all locations over the specimens (represented by the grey points) are also plotted in Fig. 12(b) in addition to the average thickness calculated for each contour (represented by the red line). The histograms reveal that the examined geometric properties of WAAM specimens generally follow a normal distribution. The statistical parameters are reported in Table 5, where s_X and V_X represent the standard deviation and coefficient of variation of the parameter X respectively. The different toolpaths examined in this study were shown to have little influence on the geometric variability, while the 45° build angle led to significantly greater variation in the cross-section breath B (measured from the two flat surfaces inclined to the build direction shown in Fig. 7), compared with those with a build angle of 90°. An exception to this is Specimen P6 (SHS 203.5×203.5×3.5), which had significantly greater variation in the outer dimensions H and B compared to the other specimens, as reflected by the notably higher values of s_H and s_B. This is because Specimen P6, which was the most slender of the studied cross-sections, contained pronounced geometric imperfections in the form of the typical local buckling mode for a SHS; this is discussed in more detail in Section 4.5.

To quantitatively evaluate the precision of the current WAAM process, the key dimensions of the WAAM parts were also compared with the corresponding nominal values, as plotted in the red dash-dotted lines in Fig. 12. The mean thicknesses of the WAAM members were shown to be greater than the nominal values for all specimens except S1. For the outer dimensions H and B, the measured values were lower than the nominal values in most cases, and the differences tended to increase as the dimensions became larger, which was likely to be a result of the thermal contractions in the cooling stage.

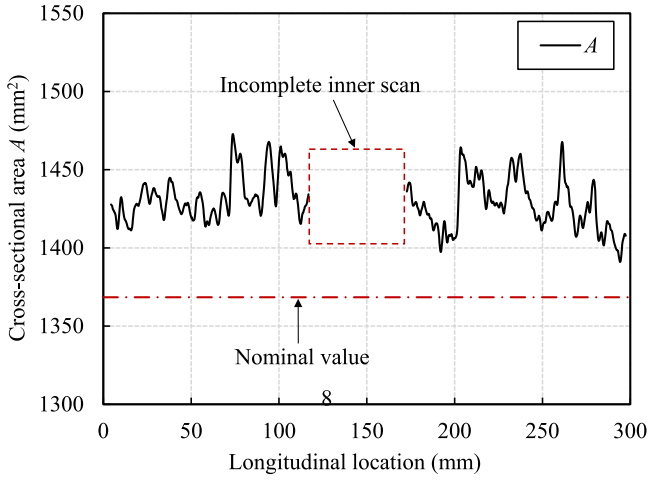
For the two stiffened SHS — S1 and S2, the mean cross-section profiles were obtained by averaging all contours at 0.2 mm intervals



(a) Cross-section height H and breadth B

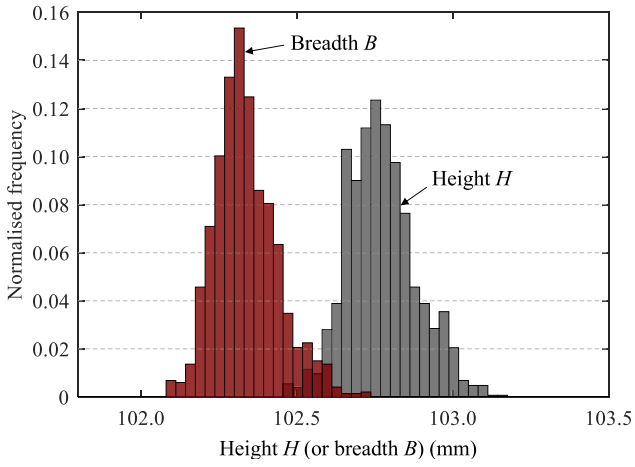


(b) Thickness t

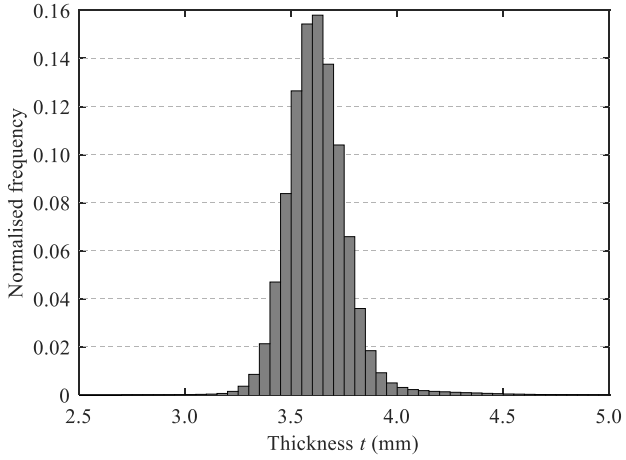


(c) Cross-sectional area A

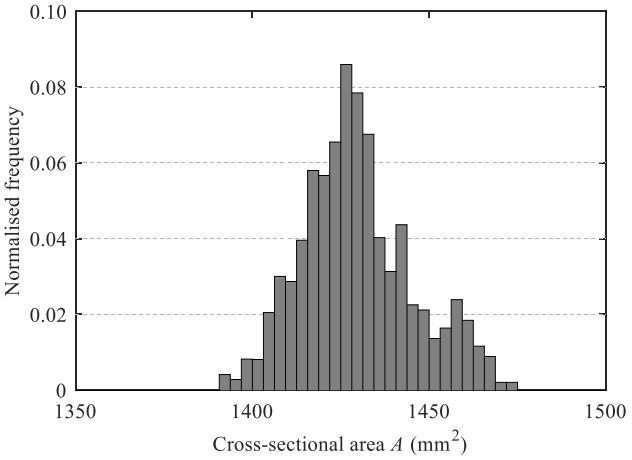
Fig. 12. Typical distributions of key geometric parameters along longitudinal axis for Specimen P3: (a) cross-section height H and breadth B, (b) thickness t and (c) cross-sectional area A.



(a) Height H and breadth B



(b) Thickness t



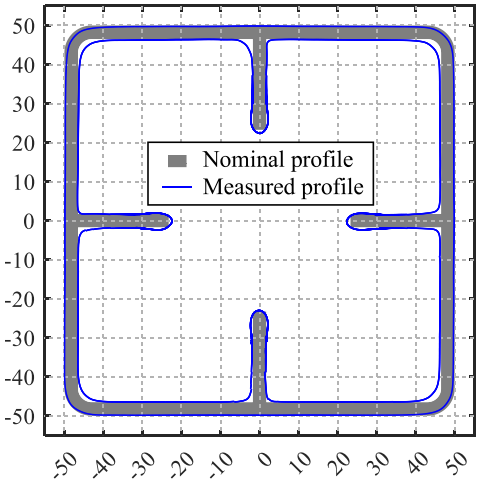
(c) Cross-sectional area A

Fig. 13. Typical histograms of key geometric parameters for Specimen P3: (a) cross-section height H and breadth B, (b) thickness t and (c) cross-sectional area A.

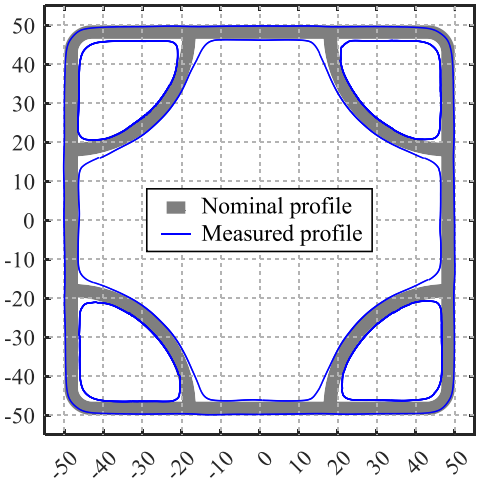
along the length, as plotted against the corresponding nominal cross-section profiles in Fig. 14. Overall, the printed profiles agreed well with the nominal profiles, except for the joint regions between the SHS and the stiffeners, where the WAAM process generally led to rounded corners as opposed to the sharp corners specified in the nominal profiles.

Table 6
Measured local geometric imperfection amplitudes of WAAM stub column specimens.

Specimen ID	Cross-section	Cross-section imperfection ω_c (mm)					Longitudinal imperfection ω_l (mm)				
		Plate 1	Plate 2	Plate 3	Plate 4	Overall	Plate 1	Plate 2	Plate 3	Plate 4	Overall
P1	58×58×8	0.11	0.15	0.11	0.20	0.20	0.30	−0.49	−0.27	−0.30	−0.49
P2	53.5×53.5×3.5	−0.26	−0.17	0.16	−0.13	−0.26	−0.26	0.26	−0.21	0.34	0.34
P3	103.5×103.5×3.5	0.61	0.34	0.53	0.88	0.88	0.47	−0.30	0.57	0.82	0.82
P4	103.5×103.5×3.5	−0.50	−0.49	0.97	−1.60	−1.60	0.38	0.27	1.98	−1.01	1.98
P5	158×158×8	0.45	0.55	0.44	0.43	0.55	0.83	−0.37	−0.38	0.92	0.92
P6	203.5×203.5×3.5	5.25	5.23	−5.06	−4.87	5.25	6.59	6.61	−6.32	−6.66	−6.66
S1	100×100×3.5 (plate stiffened)	0.62	0.57	0.88	0.52	0.88	0.47	0.52	0.77	0.86	0.86
S2	100×100×3.5 (corner stiffened)	0.78	0.50	0.69	0.75	0.78	0.71	0.72	0.68	0.43	0.72



(a) Specimen S1 (plate stiffened)



(b) Specimen S2 (corner stiffened)

Fig. 14. Average cross-section profiles (scales in mm) obtained from scanned data for (a) Specimen S1 and (b) Specimen S2.

4.5. Local geometric imperfections

The local geometric imperfections in the flat constituent plates of the examined WAAM SHS specimens, which can impact their local buckling responses under compressive loading, were analysed using the scanned data. The point cloud data of the outer surfaces were initially filtered by means of a moving average to minimise the influence of the surface undulations, as distinct for the local geometric imperfections. A sensitivity study on the filter size was carried out, as shown in Figs. 15 and 16 (where the cross-section and longitudinal imperfection amplitudes are defined in the following paragraph). It was found that square filters with a window of 8×8 mm for the specimens with t = 3.5 mm and 12×12 mm for those with t = 8 mm, corresponding to a total height of approximately eight print layers, were suitable for eliminating the surface undulations, while preserving the characteristics of the local geometric imperfections.

Cross-section and longitudinal imperfections, as defined in [50], were derived from the filtered point cloud data, with typical distributions shown in Figs. 17 and 18 for those with 90° and 45° build angles respectively. The cross-section and longitudinal imperfection amplitudes, denoted by ω_c and ω_l respectively, were taken as the 99.5th percentile deviation (rather than the maximum value) across the examined flat region to avoid the influence of particularly prominent weld beads and data noise. For each specimen, the imperfection amplitudes for each of the four constituent plates (Plates 1–4), along with the maximum overall amplitude, are reported in Table 6, where positive and negative values correspond to outward and inward deviations respectively. Unlike conventionally-produced SHS profiles, in which local geometric imperfections often have relatively long wavelengths [50,51], the examined WAAM SHS specimens typically contain local imperfections with a series of short waves running along the build direction, as shown in Figs. 17(a) and 17(b). For Specimen P6, which has the highest width-to-thickness ratio, the geometric imperfections resemble the typical elastic plate buckling shape with significantly higher magnitudes than the other specimens (Fig. 17(c)). This was likely to be the result of local buckling under the thermal-induced residual stresses generated during the printing of the specimen, and would be expected to be detrimental to the local buckling performance. For Specimen P4 with the 45° build angle, as shown in Fig. 18, greater longitudinal imperfections were observed in the flat faces inclined to the build direction compared with those parallel to the build direction, indicating lower geometric accuracy when printing along an inclined direction.

The derived geometric imperfection amplitudes for the examined WAAM specimens are plotted against the corresponding outer dimensions in Fig. 19. Since there is no guidance available on the geometric tolerances of WAAM parts at present, the plate concavity/convexity limit for hot-rolled SHS – H/100 or B/100, as specified in EN 10210-2:2019 [52], is adopted herein for comparison. All the WAAM SHS specimens with a 90° build angle, except Specimen P6, are shown to meet the requirement. Comparisons are also made with the previous measurements of longitudinal imperfections for WAAM stainless steel SHS stub columns [23], together with the characteristic imperfection amplitude of 3 mm (95% confidence) established in [23] based on the obtained data. Overall, the geometric imperfections in the WAAM specimens examined in this study are considerably lower and more consistent in magnitude than those reported in [23], reflecting the constantly improving part quality from the rapidly evolving WAAM technology.

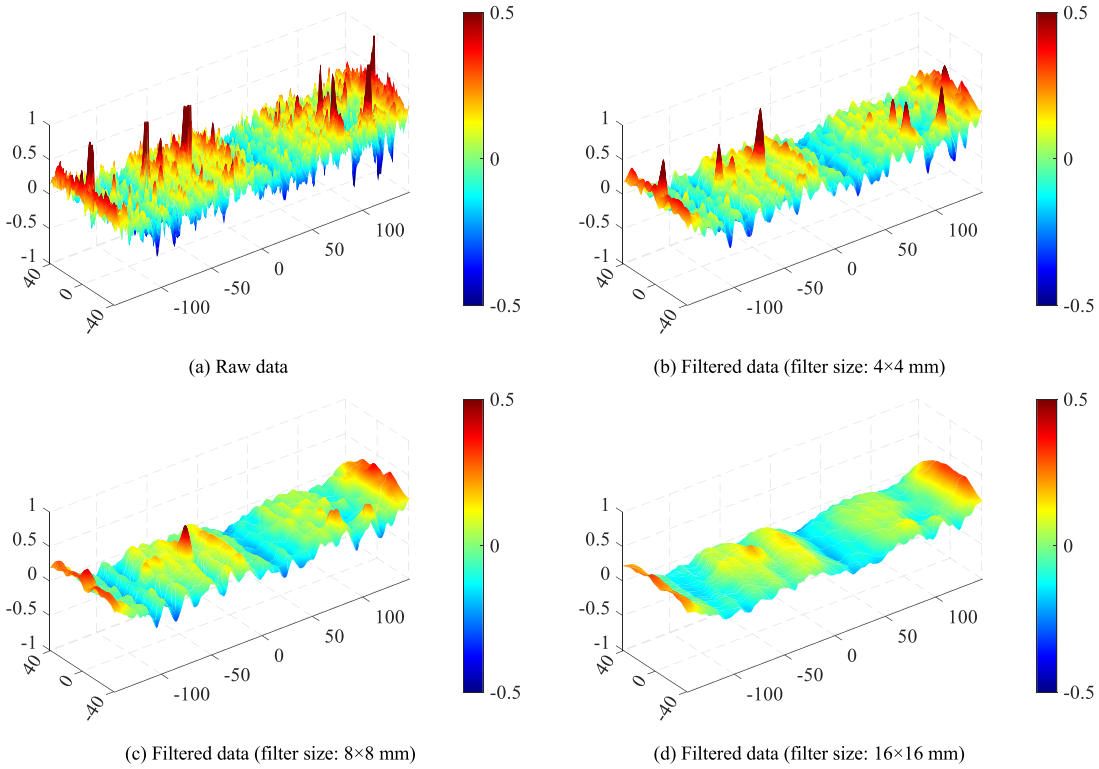


Fig. 15. Typical point cloud data for Specimen P3 (t = 3.5 mm) before and after filtering with different filter sizes (all units in mm).

Table 7
Mechanical properties of 8-mm-thick double-pass printed WAAM steels from previous tensile coupon tests on as-built material [16].

Interpass temperature (°C)	θ (°)	E (N/mm^2)	f_y (N/mm^2)	f_u (N/mm^2)	ε_u (%)	ε_f (%)
350	0	205300	709.4	764.3	8.3	19.4
	22.5	203800	663.5	760.7	9.1	19.9
	45	201100	636.9	739.2	7.2	13.9
	67.5	201800	632.5	744.0	7.8	11.8
	90	198800	615.2	734.6	7.3	9.9
150	0	208350	750.4	799.6	5.3	17.0
	22.5	207400	757.7	813.2	6.9	17.9
	45	203700	711.6	777.5	5.2	11.6
	67.5	201200	682.9	740.2	3.6	7.4
	90	199950	677.3	747.5	4.7	9.2

5. Experiments

5.1. General

The primary aims of the experimental programme were to investigate the local buckling responses of WAAM steel SHS and to verify the increased structural efficiency of the optimised stiffened SHS profiles. Auxiliary tensile coupon tests were initially carried out to obtain the mechanical properties of the examined WAAM materials. A total of eight SHS profiles, including six plain (i.e. unstiffened) SHS and two with optimised stiffeners, was tested under axial compression with fixed-ended boundary conditions.

5.2. Material tests

The mechanical properties of 8 mm-thick WAAM steel, printed with double passes and interpass temperatures of 150 °C and 350 °C, have been investigated through as-built and machined (i.e. with the surface undulations removed through machining) tensile coupon tests in a previous study [16]; the key test results are presented herein. The engineering stress-strain curves obtained from the as-built and machined coupon tests are plotted in Figs. 20 and 21 respectively, where the specimen labels begin with the printing strategy H2 or L2 (representing double pass printing with an interpass temperature of 350 °C or 150 °C respectively), followed by the angle between the loading direction and the print layer orientation θ (in °), and end with 1, 2 (representing the repeated as-built coupon tests) or M (representing the machined coupon tests). The mechanical properties for the as-built (averaged from the repeated tests) and machined coupons are shown in Tables 7 and 8 respectively, where E is the Young's modulus, f_y is the yield strength (taken as the 0.2% proof strength), f_u is the ultimate tensile strength, ε_u is the strain at the ultimate tensile strength and ε_f is the percentage elongation at fracture based on the standard gauge length. The machined coupon test results revealed nearly isotropic behaviour; the ductility was shown to be comparable to the conventionally produced steels in similar grades [53,54], and also to satisfy

Table 8
Mechanical properties of 8-mm-thick double-pass printed WAAM steels from previous tensile coupon tests on machined material [16].

Interpass temperature (°C)	θ (°)	E (N/mm^2)	f_y (N/mm^2)	f_u (N/mm^2)	ε_u (%)	ε_f (%)
350	0	205300	669.2	772.2	11.2	23.4
	22.5	207200	649.7	778.6	9.8	23.2
	45	205200	660.8	781.5	9.5	22.0
	67.5	208800	657.2	786.5	9.9	19.0
	90	207500	641.9	794.9	9.6	17.6
150	0	205300	741.7	789.6	8.6	22.2
	22.5	207200	759.4	814.4	7.0	20.1
	45	206100	740.7	806.2	5.2	17.4
	67.5	205300	740.9	805.7	4.2	13.9
	90	206000	729	793.4	6.5	17.3

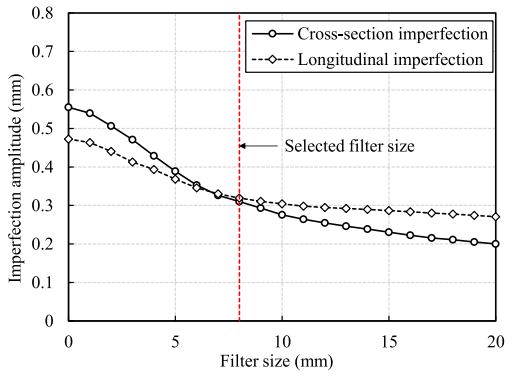


Fig. 16. Sensitivity of imperfection amplitudes (99.5th percentile values) to filter sizes for a typical flat surface from Specimen P3.

the ductility requirements for elastic global analysis specified in prEN 1993-1-1:2020 [55]. In the as-built tensile coupon tests, on the other hand, a significant reduction in both strength and ductility from the corresponding machined properties, particularly at higher angles to the print layer orientation θ, was observed, as a result of the increasing influence of the surface undulations. Microstructural characteristics of the test materials were also examined through electron backscatter diffraction (EBSD) analysis, and a typical forescatter diode (FSD) image and inverse pole figure map for the H2 material (i.e. printed with double passes and a 350 °C interpass temperature) are presented in Fig. 22. The microstructural analysis revealed a weak crystallographic texture, corresponding to the largely isotropic behaviour found in the mechanical tests; this is consistent with the findings from a previous study on similar WAAM carbon steels [13]. Further details of the abovementioned material tests on 8 mm-thick WAAM carbon steel sheet materials are reported in [16].

In the present study, the SHS specimens with the 8 mm-thick walls were manufactured using effectively the same process parameters as those tested by [16], except that the interpass temperature was set to 250 °C; hence, representative material properties were estimated based on a linear interpolation between the previous coupon test results. The relevant material properties are summarised in Table 9, where the angle between the loading direction and the print layer orientation θ coincided with the build angle φ for the stub columns examined herein.

Additional tensile coupon tests on the 3.5 mm-thick WAAM steel were carried out in this study following the same procedure as described in [16]. As-built coupon specimens were extracted at 90° and 45° to the print layer orientation from a 3.5 mm-thick WAAM steel SHS sample. Two coupon specimens were extracted and tested for each angle θ; in total, four as-built tensile coupon tests were performed in compliance with ISO 6892-1:2019 [56]. The coupon specimens were labelled by TC (tensile coupon), followed by the angle to the print layer orientation θ (in °), and finally a number indicating the location from where the coupons were extracted (1 or 2 representing locations away from or close to the initial print layers respectively).

The obtained stress-strain curves from the tensile coupon tests are plotted in Fig. 23, and the key mechanical properties are summarised in Table 9. The Young's modulus E and yield strength f_y were shown to be very similar for different θ angles, whereas a higher degree of variation in ductility was observed due to the influence of the surface undulations, which is consistent with the findings for 3.5 mm-thick WAAM carbon steels reported in [13]. Comparing the test results for coupons extracted from different locations, it is clearly shown that the thermal history has a marked effect on the mechanical properties of the as-printed materials, which is also consistent with the findings in [13,16]. The mean values were adopted to represent the material properties of the examined 3.5 mm-thick SHS specimens.

5.3. Stub column tests

The stub column tests were conducted using an Instron 3500 kN hydraulic testing machine, as shown in Fig. 24. The WAAM stub column specimens were placed between a pair of hardened high strength steel end plates, and a ball seating was employed at the top to accommodate any out-of-squareness of the specimen ends. Two stereo digital image correlation (DIC) systems, each consisting of two cameras, were adopted to monitor the strain and displacement fields and the end shortening of the test specimens; the DIC cameras were positioned along the diagonals of the SHS specimens, as illustrated in Fig. 25, enabling the deformation of all four flat faces to be captured. Speckle patterns were applied to the entire outer surface of the test specimens. Additional LED lights were used to improve the intensity and uniformity of illumination over the monitored surfaces for better quality DIC measurements.

The test machine was driven under displacement control at a rate equivalent to an average strain rate of 0.1% min^{-1}. The DIC images, together with the load and machine displacement data, were recorded at a frequency of 2 Hz using Davis 10 [57]. The DIC images were processed and analysed also using Davis 10 [57].

The load-end shortening curves obtained from the stub column tests are shown in Fig. 26, where N is the applied axial load and δ is the true end shortening extracted from the DIC data. To enable direct comparisons between stub column responses, the load-end shortening curves are plotted in a normalised form in Fig. 27, where N_{pl} is the plastic load equal to the product of the cross-sectional area measured using the weight and density $A_{density}$ and the yield strength f_y derived from the corresponding as-built coupon tests, and δ_y is the theoretical end shortening at first yield, as given by Eq. (3). A summary of the key stub column test results is provided in Table 10, where δ_u is the end shortening at the ultimate load.

$$\delta_y = \frac{f_y L}{E} \tag{3}$$

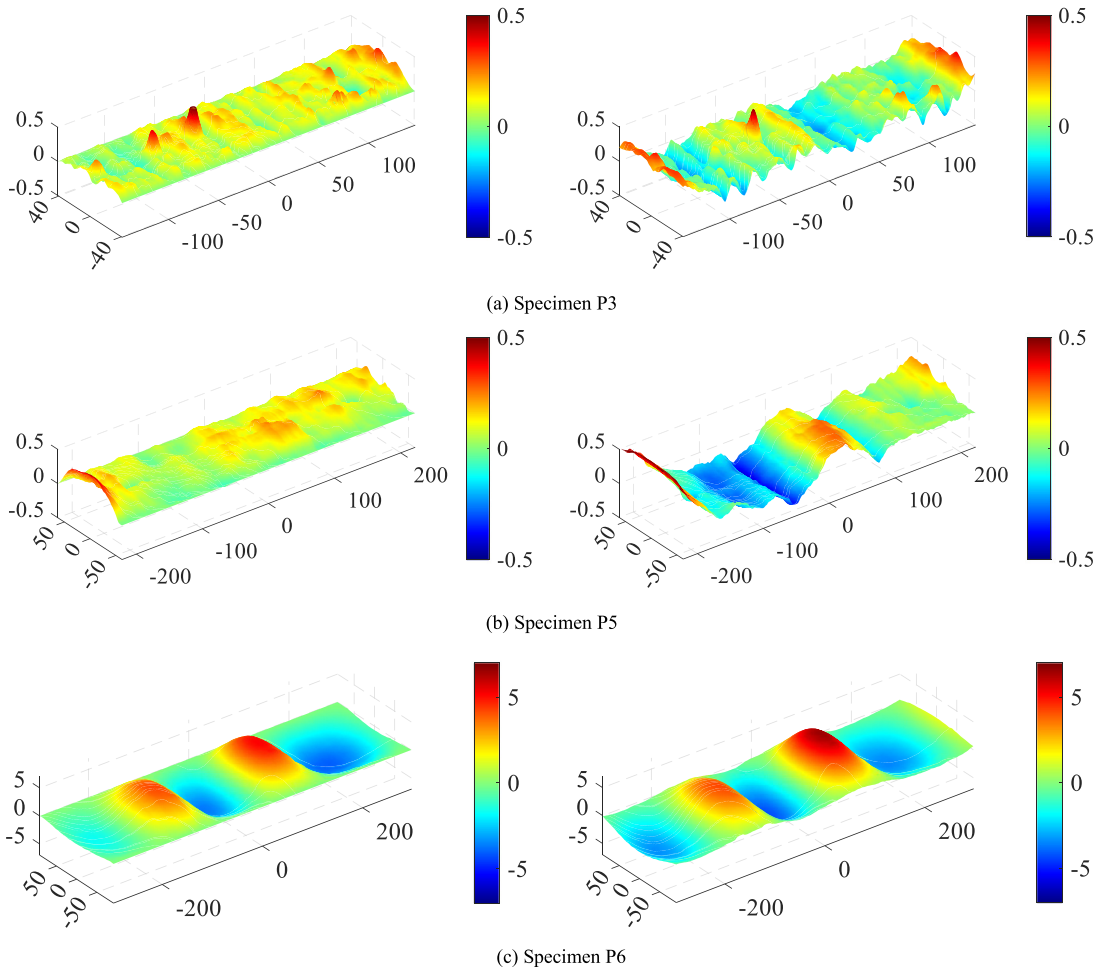


Fig. 17. Typical distributions of cross-section (left) and longitudinal (right) imperfections in WAAM stub columns with 90° build angle: (a) Specimen P3, (b) Specimen P5 and (c) Specimen P6 (all units in mm).

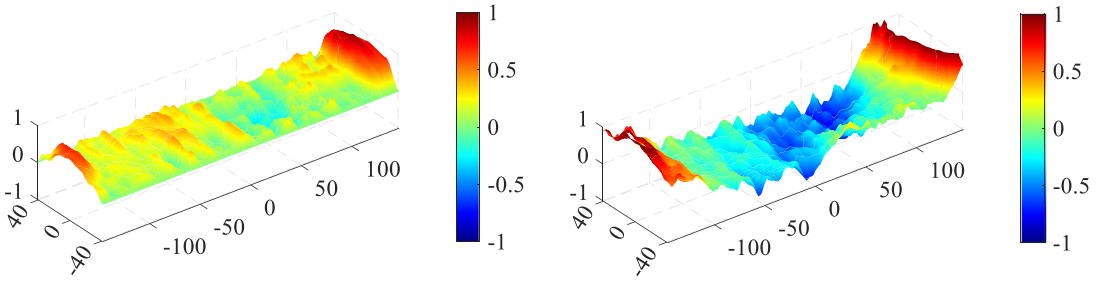
Table 9
As-built mechanical properties of WAAM steels from tensile coupon tests.

t (mm)	θ (°)	Toolpath	Specimen ID	E (N/mm^2)	f_y (N/mm^2)	f_u (N/mm^2)	ε_u (%)	ε_f (%)
3.5	90	Single pass	TC-90–1	199200	587.1	753.0	10.0	14.5
			TC-90–2	206500	715.0	790.1	7.1	16.5
			Mean	202900	651.0	771.6	8.6	15.5
3.5	45	Single pass	TC-45–1	208600	613.5	719.1	5.9	9.7
			TC-45–2	204800	710.1	787.1	6.8	13.2
			Mean	206700	661.8	753.1	6.4	11.4
8	90	Double pass	Mean	199400	646.3	741.0	6.0	9.6

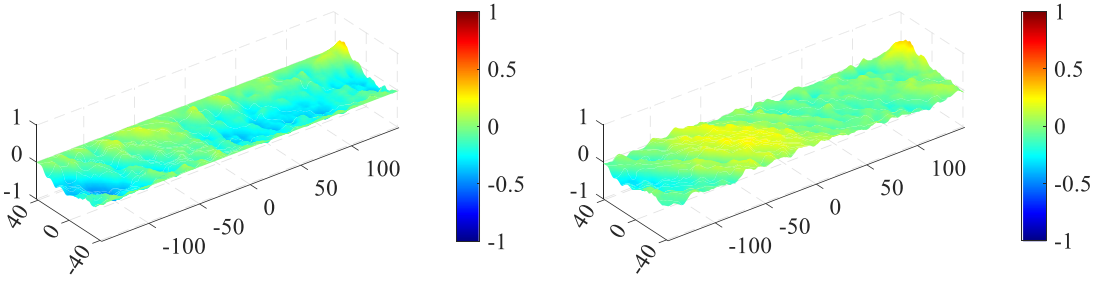
Table 10
Summary of WAAM stub colum test results.

Specimen ID	Cross-section	Toolpath	φ (°)	N_{pl} (kN)	N_u (kN)	δ_u (mm)	N_u/N_{pl}
P1	58×58×8	Double pass	90	1033.1	1609.2	22.20	1.558
P2	53.5×53.5×3.5	Single pass	90	451.1	524.0	2.89	1.161
P3	103.5×103.5×3.5	Single pass	90	899.1	784.6	1.34	0.873
P4	103.5×103.5×3.5	Single pass	45	958.4	759.5	1.28	0.793
P5	158×158×8	Double pass	90	3070.0	3195.5	4.07	1.041
P6	203.5×203.5×3.5	Single pass	90	1823.5	698.3	3.40	0.383
S1	100×100×3.5 (plate stiffened)	Single pass	90	1060.2	1169.6	2.82	1.103
S2	100×100×3.5 (corner stiffened)	Single pass	90	1290.2	1480.0	4.64	1.147

Overall, the initial slopes of all normalised load-end shortening curves agree well with the theoretical value, as represented by the black dashed line in Fig. 27, except for Specimen P6, which exhibited a stiffness akin to the post-buckled value due to the influence of the residual stresses and local geometric imperfections. For the plain SHS,

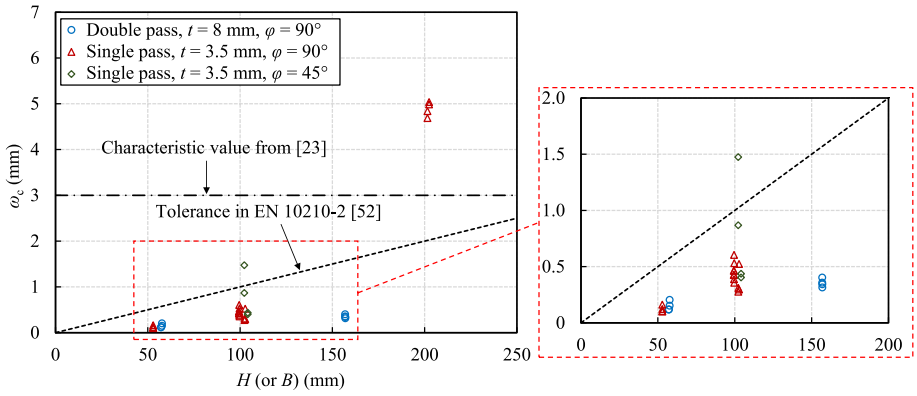


(a) Face inclined to build direction

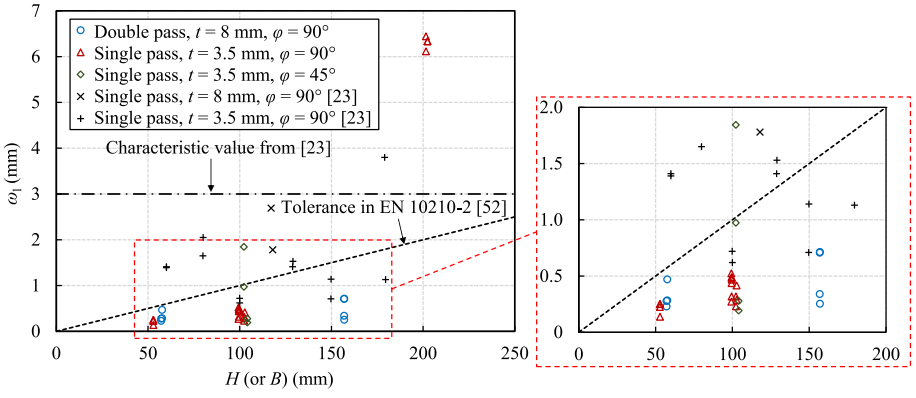


(b) Face parallel to build direction

Fig. 18. Typical distributions of cross-section (left) and longitudinal (right) imperfections in Specimen P4 with 45° build angle: (a) face inclined to build direction and (b) face parallel to build direction (all units in mm).

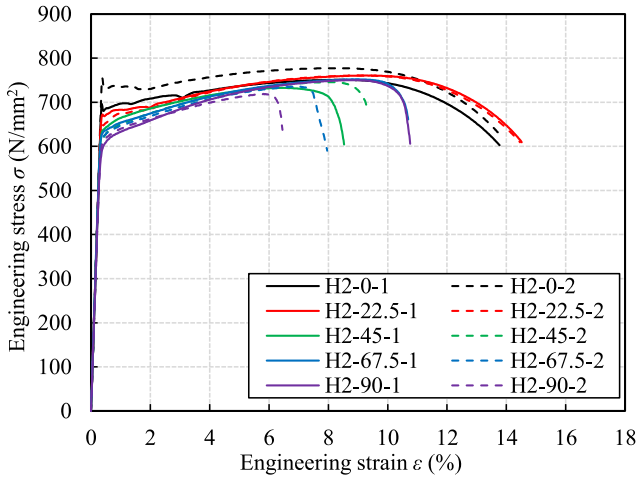


(a) Cross-section imperfections ω_c

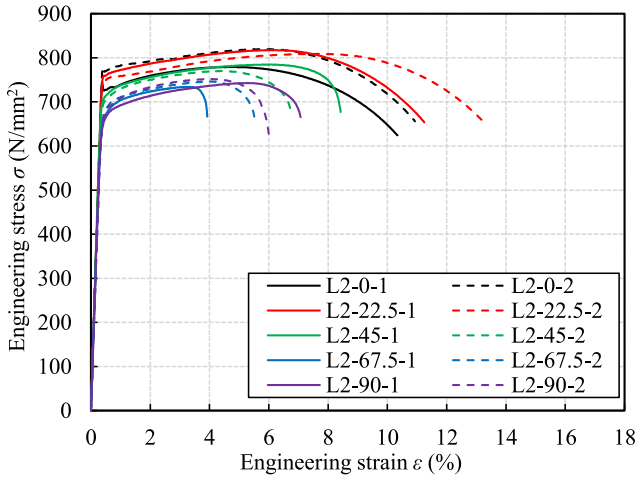


(b) Longitudinal imperfections ω_l

Fig. 19. Comparisons of measured local geometric imperfections in WAAM stub columns with characteristic value from existing measurements [23] and tolerance for hot-rolled SHS [52].

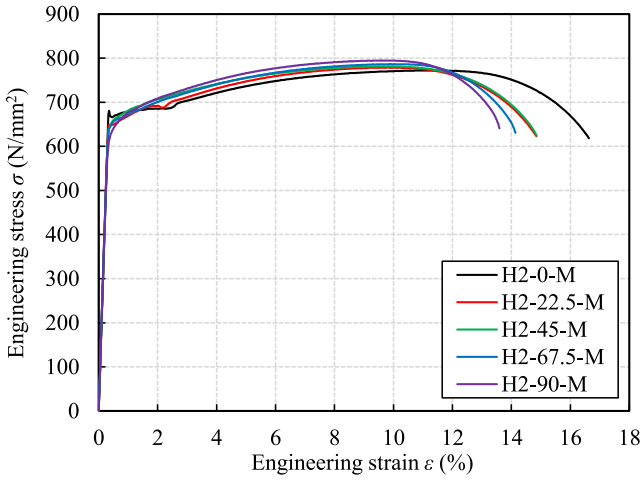


(a) Interpass temperatrure = 350 °C

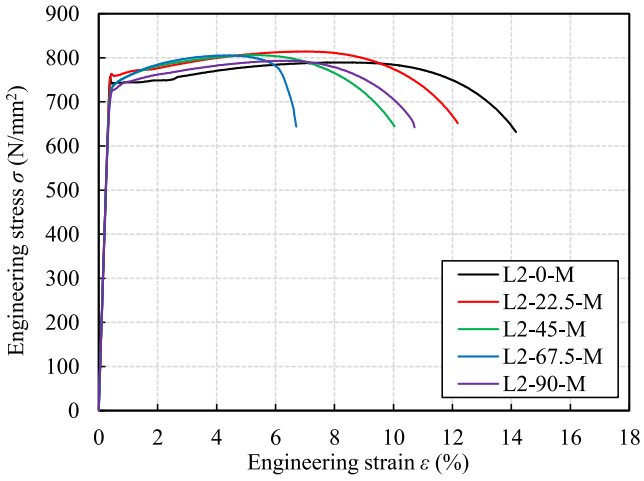


(b) Interpass temperatrure = 150 °C

Fig. 20. Stress-strain curves for 8 mm-thick WAAM steels obtained from previous tensile coupon tests on as-built material [16].



(a) Interpass temperatrure = 350 °C



(b) Interpass temperatrure = 150 °C

Fig. 21. Stress-strain curves for 8 mm-thick WAAM steels obtained from previous tensile coupon tests on machined material [16].

as expected, the load-carrying capacity tended to reduce as the width-to-thickness ratio increases. With the same nominal profile, the ultimate load for Specimen P4 ($\varphi = 45°$) was lower than that for Specimen P3 ($\varphi = 90°$) by 9.5% as a result of the increased geometric imperfections when printing along an inclined direction.

Compared with the plain SHS — Specimen P3, which has a similar outer profile to the two stiffened SHS, Specimen S1 (i.e. plate-stiffened) has 49.1% higher load-carrying capacity with an increase of 17.9% in cross-sectional area, while Specimen S2 (i.e. corner-stiffened) achieved an enhancement of 88.6% in load-carrying capacity with an increase of 43.5% in cross-sectional area. A significant increase in deformation capacity was also achieved by the two stiffened SHS, as reflected by the notably higher values of δ_u than that for Specimen P3. Overall, a disproportionate improvement in the structural performance relative to the increase in mass was achieved, showing that optimised structural elements are a viable and efficient means of exploiting the geometric freedom of WAAM.

All tested WAAM stub column specimens are displayed in Fig. 28. The plain SHS specimens failed in the classic plate local buckling shape, while the two stiffened SHS exhibited distinct failure modes — Specimen S1 (plate-stiffened) buckled with two half-waves across one flat face, while Specimen S2 (corner-stiffened) failed by outward bulging resembling the elephant foot failure mode. For Specimen S2, localised fracture occurred, in the post-ultimate stage, at the junction between the SHS and one of the corner stiffeners within the most heavily deformed local buckling region, as shown in Fig. 29; this did not affect the ultimate load-carrying capacity of the test specimen, but did indicate inferior mechanical properties at the intersections. Typical out-of-plane displacement fields in the post-ultimate stage from the DIC data are shown in Fig. 30, where the different failure modes of the plain and stiffened SHS can be quantitatively visualised.

6. Comparisons with existing test data and design predictions

6.1. General

In this section, the freshly generated WAAM stub column test data are compared with existing test data on conventionally-produced steel SHS stub columns to evaluate the influence of the unique geometric and mechanical properties inherent to the WAAM process. Comparisons are also made against the resistance predictions from the existing Eurocode 3 structural design rules to assess their suitability for application to WAAM elements.

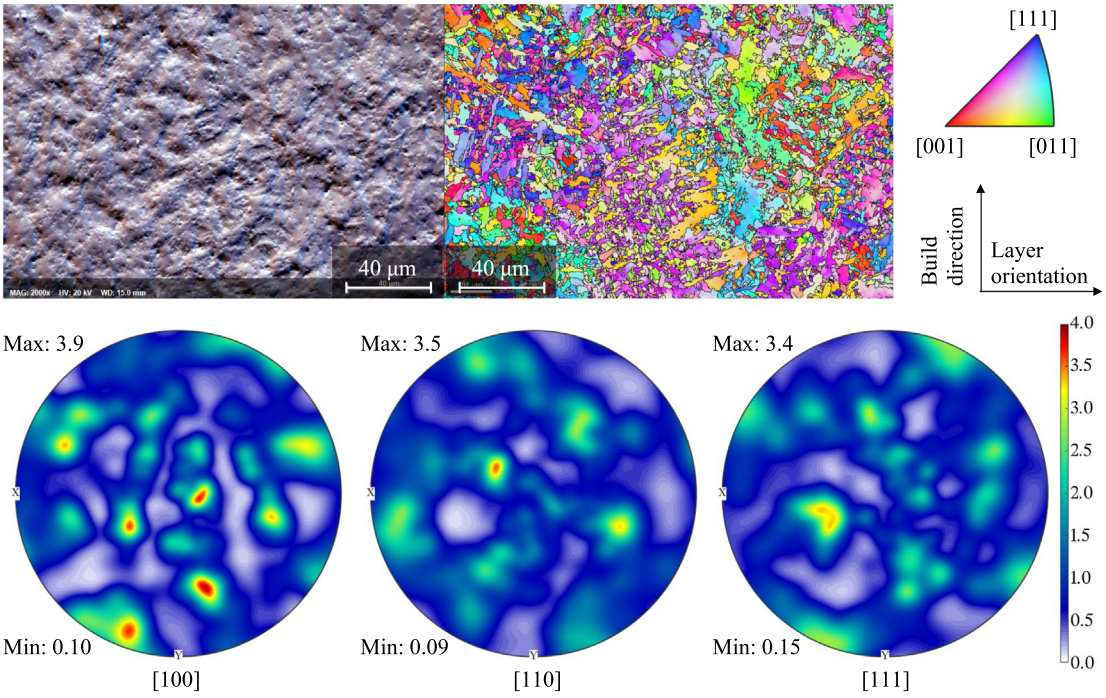


Fig. 22. Typical FSD image, inverse pole figure map and pole figures of ferrite phase of machined samples extracted from H2 material.

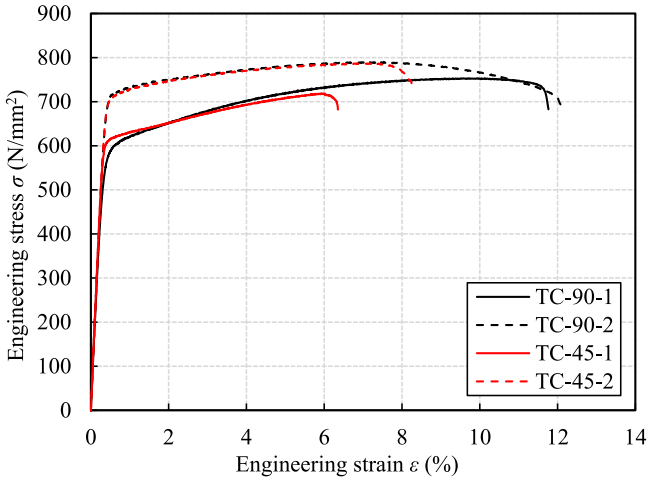


Fig. 23. As-built stress-strain curves for 3.5 mm-thick WAAM steels obtained from tensile coupon tests.

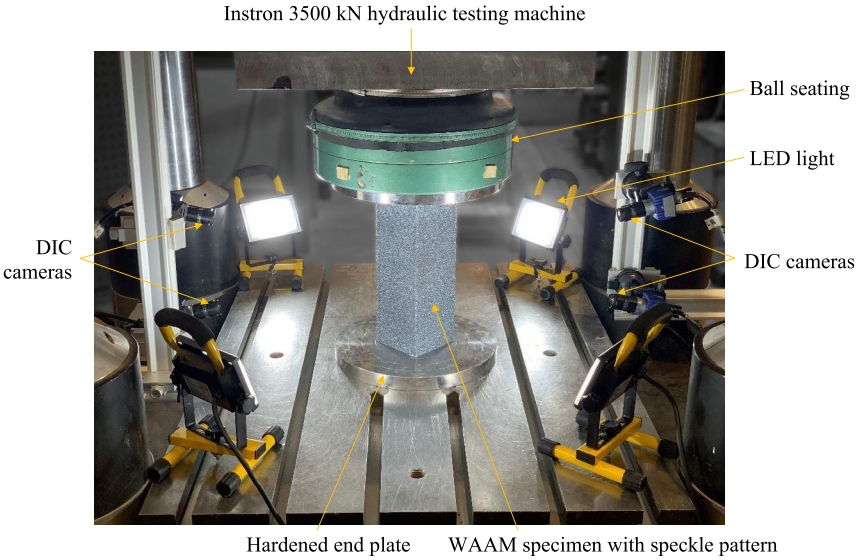


Fig. 24. WAAM SHS stub column test setup.

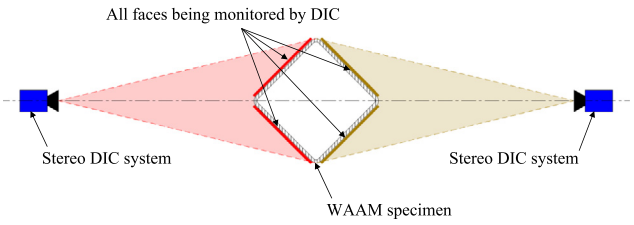
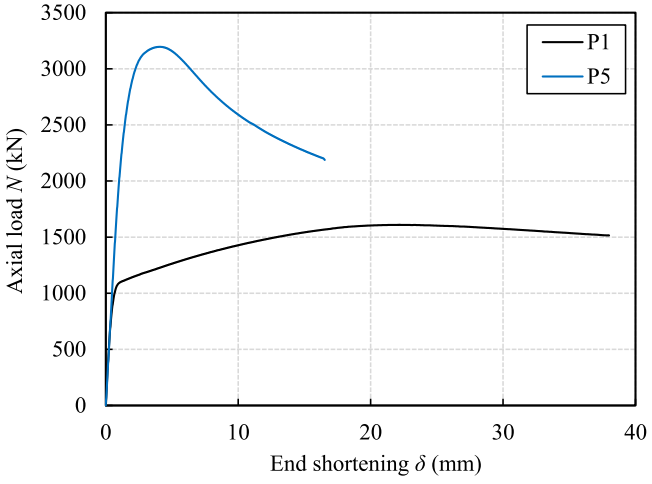
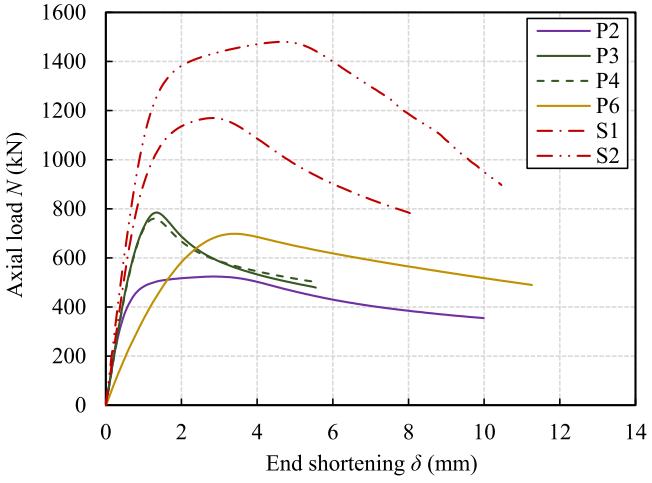


Fig. 25. Plan view of DIC setup.



(a) 8 mm-thick specimens



(b) 3.5 mm-thick specimens

Fig. 26. Load-end shortening curves obtained from stub column tests for (a) 8-mm thick specimens and (b) 3.5 mm-thick specimens.

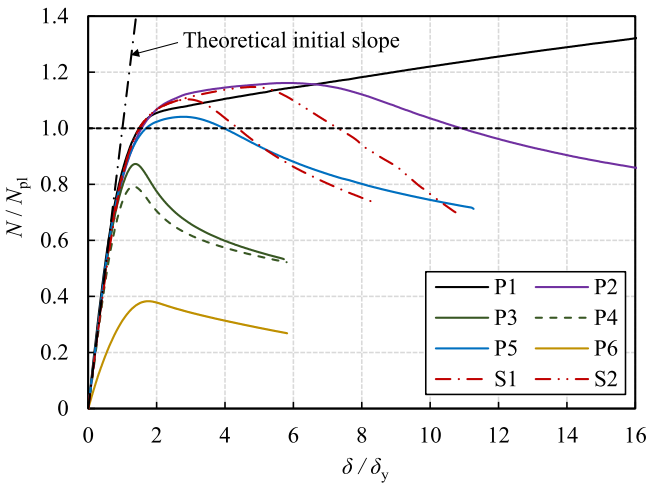


Fig. 27. Normalised load-end shortening curves obtained from stub column tests.



Fig. 28. Failure modes of WAAM stub columns.

6.2. Comparisons with conventionally-produced SHS

A total of 179 stub column test data collected from the literature, consisting of 36 on hot-rolled steel SHS [50,53,58–61] and 143 on cold-formed steel SHS [53,59–75], are plotted together with the WAAM stub column data in Fig. 31, where $\overline{\lambda}_p = \sqrt{f_y/f_{cr}}$ is the relative local slenderness and f_{cr} is the elastic critical local buckling stress. For the plain SHS, f_{cr} is taken as the elastic local buckling stress of the constituent plates, while for the two stiffened SHS, f_{cr} is obtained using the numerical software CUFSM [40]. The Winter curve, as specified in prEN 1993-1-5:2022 [76], is also plotted in Fig. 31 for reference. Note that the as-built material properties for the WAAM SHS are used in the calculations, which incorporate the weakening effect of the geometric undulations inherent to WAAM and were found previously to be appropriate for use with conventional structural design methods [23,26]. Overall, the data points for the WAAM stub columns generally follow the trend of the conventionally-rolled SHS data. However, in the intermediate (i.e. near $\overline{\lambda}_p = 0.673$) and the slender ranges, the WAAM SHS data fall below the majority of the conventionally-rolled SHS data, indicating the potentially marginally inferior local buckling performance of WAAM elements relative to conventional elements.

6.3. Assessment of EC3 design method

The applicability of the Eurocode 3 (EC3) design rules to WAAM SHS is assessed herein. For axial compression, the cross-section is initially classified as either Class 1–3 (i.e. stocky) or Class 4 (i.e. slender)

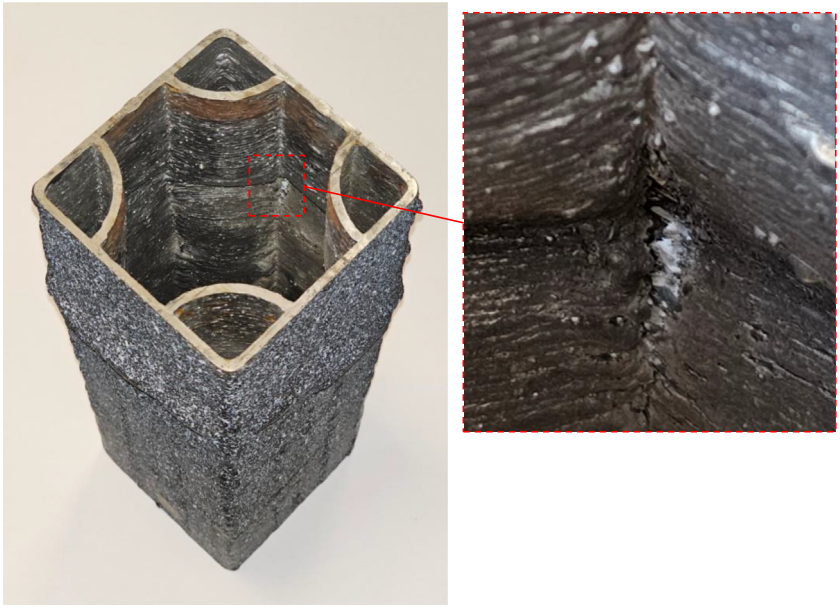


Fig. 29. Localised fracture at junction between SHS and a corner stiffener for Specimen S2.

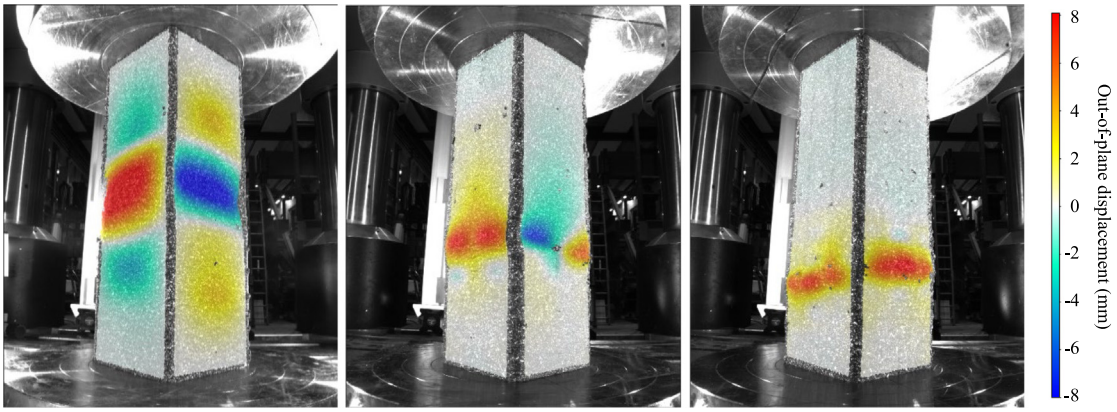


Fig. 30. Typical out-of-plane displacement fields obtained from DIC results for Specimens P3 (left), S1 (middle) and S2 (right) in post-ultimate stage.

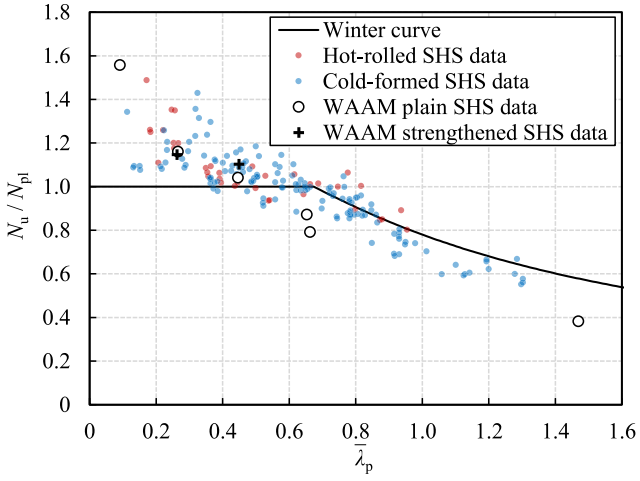


Fig. 31. Comparisons of WAAM stub column test data with existing stub column data on conventionally-produced SHS.

according to the Class 3 slenderness limit of $c/t\varepsilon = 38$, as specified in the latest revision to EC3 – prEN 1993-1-1:2020 [55], where c is the width of the flat portion of the cross-section faces and $\varepsilon = \sqrt{235/f_y}$. The design resistance $N_{c,Rd}$ is given by Eqs. (4) and (5), where A is taken equal to $A_{density}$, f_y is taken as the yield strength from the as-built coupon tests, $N_{c,R}$ is the unfactored resistance, A_{eff} is the effective area calculated in accordance with EN 1993-1-5:2022 [76], and γ_{M0} is the partial safety factor taken equal to unity for carbon steels.

$$N_{c,Rd} = \frac{N_{c,R}}{\gamma_{M0}} = \frac{A f_y}{\gamma_{M0}} \quad \text{for Class 1–3 cross-sections} \tag{4}$$

$$N_{c,Rd} = \frac{N_{c,R}}{\gamma_{M0}} = \frac{A_{eff} f_y}{\gamma_{M0}} \quad \text{for Class 4 cross-sections} \tag{5}$$

The ultimate loads derived from the stub column tests $N_{u,test}$ are normalised by the unfactored resistances $N_{c,R}$ and plotted against the plate slenderness $c/t\varepsilon$ in Fig. 32. The current Class 3 slenderness limit appears to be unsafe for the WAAM steel SHS. In the very stocky range, the EC3 resistance predictions are overly conservative in general due to the lack of account for strain hardening [77,78], while in the slender range, the EC3 method overpredicts the local buckling resistances of WAAM SHS by up to 36.8%. It should be noted that this finding is made based on a limited number of test data (and that further experimental results are required), but nonetheless points to the need for new slenderness

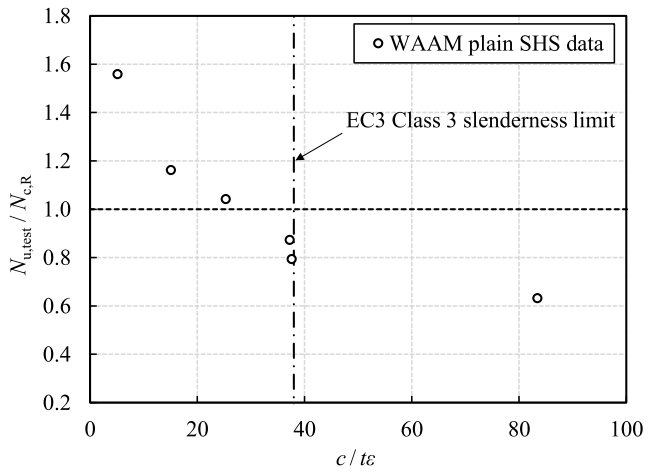


Fig. 32. Comparisons of WAAM plain SHS stub column test data with EC3 slenderness limit and resistance predictions.

limits and a new plate buckling curve for compressed WAAM cross-sections. Additionally, it is worth mentioning that several experimental studies have been devoted to investigating the local buckling behaviour of WAAM curved-walled sections, such as circular hollow sections [24] and irregular shaped hollow sections [25]; further experimental work, as well as the development of suitable structural design rules for WAAM curved elements, is also imperative.

7. Conclusions

The behaviour of wire arc additively manufactured (WAAM) stub columns with standard and optimised square hollow section (SHS) profiles has been investigated and presented in this paper. An elastic buckling stress-based optimisation study was initially carried out to explore the optimal configurations of stiffeners for SHS against local buckling. A total of six plain SHS, covering a wide spectrum of width-to-thickness ratios, along with two SHS strengthened with optimised internal stiffeners, was produced via WAAM using high strength steel wire feedstock with different toolpaths and build angles. 3D laser-scanning was employed to investigate the unique undulating geometry of the WAAM specimens. Statistical analyses of the key cross-sectional dimensions were carried out, and local geometric imperfection distributions were revealed utilising the scanned data.

The WAAM stub column specimens were tested under axial compression with fixed-ended boundary conditions. After normalisation using the as-built material properties, the WAAM SHS generally had similar load-carrying capacities to conventionally-manufactured SHS in the stocky range, but tended to perform less well in the slender range. The existing Eurocode 3 design method was also shown to overpredict the local buckling resistances of slender WAAM SHS, though further test data are needed to verify this finding. Finally, the SHS strengthened with optimised stiffeners were shown to achieve a disproportionate increase in strength and deformation capacity relative to the increase in mass of the added stiffeners, demonstrating the great potential of metal AM to improve the efficiency of material use by harnessing the enhanced geometric freedom through structural optimisation.

CRediT authorship contribution statement

Xin Meng: Writing – review & editing, Writing – original draft, Visualization, Supervision, Methodology, Investigation, Formal analysis, Conceptualization. **Ben Weber:** Writing – review & editing, Visualization, Software, Investigation, Data curation. **Masashi Nitawaki:** Writing – review & editing, Resources. **Leroy Gardner:** Writing – review & editing, Supervision, Resources, Project administration, Funding acquisition, Conceptualization.

Declaration of competing interest

The authors declare that they have no known competing financial interests or personal relationships that could have appeared to influence the work reported in this paper.

Data availability

Data will be made available on request.

Acknowledgements

This research project was funded by Shimizu Corporation, Japan, and financial support was also received from the National Research Fund, Luxembourg. The authors would like to thank Stivell Hemon and Kasper Siderius from MX3D for the technical support. The authors would also like to gratefully acknowledge Les Clark, Paul Crudge and Alfredo Olivo from the Structures Laboratory at Imperial College London for their assistance in the experimental programme, and Takayuki Sagawa from Shimizu Corporation for the technical comments on the results.

References

[1] ISO/ASTM 52900:2021, Additive Manufacturing — General Principles — Fundamentals and Vocabulary, International Organization for Standardization (ISO), 2021.
[2] A. Kanyilmaz, A.G. Demir, M. Chierici, F. Berto, L. Gardner, S.Y. Kandukuri, et al., Role of metal 3D printing to increase quality and resource-efficiency in the construction sector, Addit. Manuf. 50 (2022) 102541.
[3] L. Gardner, Metal additive manufacturing in structural engineering – Review, advances, opportunities and outlook, Structures 47 (2023) 2178–2193.
[4] PAS 6012:2020, Additive Manufacturing – Wire Arc – Guide, The British Standards Institution (BSI), 2020.
[5] T. Debroy, H.L. Wei, J.S. Zuback, T. Mukherjee, J.W. Elmer, J.O. Milewski, et al., Additive manufacturing of metallic components – Process, structure and properties, Prog. Mater. Sci. 92 (2018) 112–224.
[6] L. Gardner, P. Kyvelou, G. Herbert, C. Buchanan, Testing and initial verification of the world's first metal 3D printed bridge, J. Constr. Steel Res. 172 (2020) 106233.
[7] P. Kyvelou, H. Slack, D. Daskalaki Mountanou, M.A. Wadee, T.B. Britton, C. Buchanan, et al., Mechanical and microstructural testing of wire and arc additively manufactured sheet material, Mater. Des. 192 (2020) 108675.
[8] V. Laghi, M. Palermo, L. Tonelli, G. Gasparini, L. Ceschini, T. Trombetti, Tensile properties and microstructural features of 304L austenitic stainless steel produced by wire-and-arc additive manufacturing, Int. J. Adv. Manuf. Tech. 106 (2020) 3693–3705.
[9] L. Wang, J. Xue, Q. Wang, Correlation between arc mode, microstructure, and mechanical properties during wire arc additive manufacturing of 316l stainless steel, Mater. Sci. Eng. A 751 (2019) 183–190.
[10] N. Hadjipantelis, B. Weber, C. Buchanan, L. Gardner, Description of anisotropic material response of wire and arc additively manufactured thin-walled stainless steel elements, Thin-Walled Struct. 171 (2022) 108634.
[11] V. Laghi, M. Palermo, G. Gasparini, V.A. Girelli, T. Trombetti, On the influence of the geometrical irregularities in the mechanical response of wire-and-arc additively manufactured planar elements, J. Constr. Steel Res. 178 (2021) 106490.
[12] C.V. Haden, G. Zeng, F.M. Carter, C. Ruhl, B.A. Krick, D.G. Harlow, Wire and arc additive manufactured steel: Tensile and wear properties, Addit. Manuf. 16 (2017) 115–123.
[13] C. Huang, P. Kyvelou, R. Zhang, T. ben Britton, L. Gardner, Mechanical testing and microstructural analysis of wire arc additively manufactured steels, Mater. Des. 216 (2022) 110544.
[14] V.A. Silvestru, I. Ariza, J. Vienne, L. Michel, A.M. Aguilar Sanchez, U. Angst, et al., Performance under tensile loading of point-by-point wire and arc additively manufactured steel bars for structural components, Mater. Des. 205 (2021) 109740.
[15] E. Aldalur, F. Veiga, A. Suárez, J. Bilbao, A. Lamikiz, High deposition wire arc additive manufacturing of mild steel: Strategies and heat input effect on microstructure and mechanical properties, J. Manuf. Process. 58 (2020) 615–626.
[16] B. Weber, X. Meng, R. Zhang, M. Nitawaki, T. Sagawa, L. Gardner, Tensile behaviour of WAAM high strength steel material and members, Mater. Des. (2023) submitted for publication.

[17] L. Tonelli, V. Laghi, M. Palermo, T. Trombetti, L. Ceschini, AA5083 (Al–Mg) plates produced by wire-and-arc additive manufacturing: Effect of specimen orientation on microstructure and tensile properties, Prog. Addit. Manuf. 6 (2021) 479–494.
[18] T. Klein, A. Arnoldt, R. Lahnsteiner, M. Schnall, Microstructure and mechanical properties of a structurally refined Al–Mg–Si alloy for wire-arc additive manufacturing, Mater. Sci. Eng. A 830 (2022) 142318.
[19] R. Fu, S. Tang, J. Lu, Y. Cui, Z. Li, H. Zhang, et al., Hot-wire arc additive manufacturing of aluminum alloy with reduced porosity and high deposition rate, Mater. Des. 199 (2021) 109370.
[20] F. Wang, S. Williams, P. Colegrove, A.A. Antonysamy, Microstructure and mechanical properties of wire and arc additive manufactured Ti-6Al-4V, Metall. Mater. Trans. A Phys. Metall. Mater. Sci. 44 (2013) 968–977.
[21] Y. Tian, J. Shen, S. Hu, Z. Wang, J. Gou, Microstructure and mechanical properties of wire and arc additive manufactured Ti-6Al-4V and AlSi5 dissimilar alloys using cold metal transfer welding, J. Manuf. Process. 46 (2019) 337–344.
[22] J. Gou, J. Shen, S. Hu, Y. Tian, Y. Liang, Microstructure and mechanical properties of as-built and heat-treated Ti-6Al-4V alloy prepared by cold metal transfer additive manufacturing, J. Manuf. Process. 42 (2019) 41–50.
[23] P. Kyvelou, C. Huang, L. Gardner, C. Buchanan, Structural testing and design of wire arc additively manufactured square hollow sections, J. Struct. Eng. 147 (2021) 1–19.
[24] V. Laghi, M. Palermo, G. Gasparini, V.A. Girelli, T. Trombetti, Experimental results for structural design of wire-and-arc additive manufactured stainless steel members, J. Constr. Steel Res. 167 (2020) 105858.
[25] C. Huang, X. Meng, L. Gardner, Cross-sectional behaviour of wire arc additively manufactured tubular beams, Eng. Struct. 272 (2022) 114922.
[26] C. Huang, X. Meng, C. Buchanan, L. Gardner, Flexural buckling of wire arc additively manufactured tubular columns, J. Struct. Eng. 148 (2022) 1–14.
[27] X. Guo, P. Kyvelou, J. Ye, L.H. Teh, L. Gardner, Experimental investigation of wire arc additively manufactured steel single-lap shear bolted connections, Thin-Walled Struct. 181 (2022) 110029.
[28] H. Seifi, A.Rezaee. Javan, X. Lin, Y.M. Xie, An innovative and inexpensive experimental setup for testing connections in gridshell structures, Eng. Struct. 207 (2020) 110257.
[29] H. Seifi, M. Xie, J. O'Donnell, N. Williams, Design and fabrication of structural connections using bi-directional evolutionary structural optimization and additive manufacturing, Appl. Mech. Mater. 846 (2016) 571–576.
[30] K.D. Tsavdaridis, E. Efthymiou, A. Adugu, J.A. Hughes, L. Grekavicius, Application of structural topology optimisation in aluminium cross-sectional design, Thin-Walled Struct. 139 (2019) 372–388.
[31] J. Ye, P. Kyvelou, F. Gilardi, H. Lu, M. Gilbert, L. Gardner, An end-to-end framework for the additive manufacture of optimized tubular structures, IEEE Access 9 (2021) 165476–165489.
[32] T. Tran, L.Y. Li, Global optimization of cold-formed steel channel sections, Thin-Walled Struct. 44 (2006) 399–406.
[33] Y.S. Tian, T.J. Lu, Minimum weight of cold-formed steel sections under compression, Thin-Walled Struct. 42 (2004) 515–532.
[34] P. Vinot, S. Cogan, J. Piranda, Shape optimization of thin-walled beam-like structures, Thin-Walled Struct. 39 (2001) 611–630.
[35] B. Wang, B.P. Gilbert, A.M. Molinier, H. Guan, L.H. Teh, Shape optimisation of cold-formed steel columns with manufacturing constraints using the Hough transform, Thin-Walled Struct. 106 (2016) 75–92.
[36] B.P. Gilbert, T.J.M. Savoyat, L.H. Teh, Self-shape optimisation application: Optimisation of cold-formed steel columns, Thin-Walled Struct. 60 (2012) 173–184.
[37] A. Zhu, H. Zhu, X. Zhang, Y. Lu, Experimental study and analysis of inner-stiffened cold-formed SHS steel stub columns, Thin-Walled Struct. 107 (2016) 28–38.
[38] Z. Tao, L.H. Han, Z.B. Wang, Experimental behaviour of stiffened concrete-filled thin-walled Hollow Steel Structural (HSS) stub columns, J. Constr. Steel Res. 61 (2005) 962–983.
[39] Y. Wang, Y. Yang, S. Zhang, Static behaviors of reinforcement-stiffened square concrete-filled steel tubular columns, Thin-Walled Struct. 58 (2012) 18–31.
[40] Z. Li, B.W. Schafer, Buckling analysis of cold-formed steel members with general boundary conditions using CUFSM: Conventional and constrained finite strip methods, in: 20th International Specialty Conference on Cold-Formed Steel Structures - Recent Research and Developments in Cold-Formed Steel Design and Construction, Saint Louis, Missouri, USA, 2010.
[41] MX3D, MX3D | about, 2021, Available from https://mx3d.com/company/about/. (Accessed 29 November 2021).
[42] D. Ding, C. Shen, Z. Pan, D. Cuiuri, H. Li, N. Larkin, et al., Towards an automated robotic arc-welding-based additive manufacturing system from CAD to finished part, CAD Comput. Aided Des. 73 (2016) 66–75.
[43] G. Venturini, F. Montevecchi, A. Scippa, G. Campatelli, Optimization of WAAM deposition patterns for T-crossing features, Proc. CIRP 55 (2016) 95–100.
[44] G. Venturini, F. Montevecchi, F. Bandini, A. Scippa, G. Campatelli, Feature based three axes computer aided manufacturing software for wire arc additive manufacturing dedicated to thin walled components, Addit. Manuf. 22 (2018) 643–657.
[45] L. Nguyen, J. Buhl, M. Bambach, Continuous Eulerian tool path strategies for wire-arc additive manufacturing of rib-web structures with machine-learning-based adaptive void filling, Addit. Manuf. 35 (2020) 101265.
[46] R.D. Ziemian, Guide to Stability Design Criteria for Metal Structures, sixth ed., Wiley, 2010.
[47] Geomagic Wrap 2017 [Software], 3D Systems, Inc, 2017.
[48] Matlab R2022a [Software], The MathWorks, Inc, 2022.
[49] Rhino 7 [Software], Robert McNeel & Associates, 2021.
[50] X. Meng, L. Gardner, Testing of hot-finished high strength steel SHS and RHS under combined compression and bending, Thin-Walled Struct. 148 (2020) 106262.
[51] J.H. Zhu, B. Young, Tests and design of aluminum alloy compression members, J. Struct. Eng. 132 (2006) 1096–1107.
[52] EN 10210-2:2019, Hot Finished Steel Structural Hollow Sections - Part 2: Tolerances, Dimensions and Sectional Properties, European Committee for Standardization (CEN), 2019.
[53] J. Wang, S. Afshan, N. Schillo, M. Theofanous, M. Feldmann, L. Gardner, Material properties and compressive local buckling response of high strength steel square and rectangular hollow sections, Eng. Struct. 130 (2017) 297–315.
[54] M.T. Chen, B. Young, Tests of cold-formed normal and high strength steel tubes under tension, Thin-Walled Struct. 153 (2020) 106844.
[55] prEN 1993-1-1:2020, Eurocode 3. Design of Steel Structures. Part 1-1. General Rules and Rules for Buildings, European Committee for Standardization (CEN), 2020.
[56] ISO 6892-1:2019, Metallic Materials — Tensile Testing — Part 1: Method of Test at Room Temperature, International Organization for Standardization (ISO), 2019.
[57] Davis 10 [Software], LaVision, 2019.
[58] T.J. Dwyer, Theoretical and Experimental Study of Tubular Beam–Columns (MS thesis), Fritz Laboratory Reports, 1963.
[59] B. Kato, I. Nishiyama, Local buckling strength and deformation capacity of cold-formed steel rectangular hollow section (in Japanese), Trans. Archit. Inst. Japan 294 (1980) 45–52.
[60] J. Nseir, Development of a New Design Method for the Cross-Section Capacity of Steel Hollow Sections (Ph.D. thesis), University of Liège, 2015.
[61] L. Gardner, N. Saari, F. Wang, Comparative experimental study of hot-rolled and cold-formed rectangular hollow sections, Thin-Walled Struct. 48 (2010) 495–507.
[62] J.L. Ma, T.M. Chan, B. Young, Experimental investigation on stub-column behavior of cold-formed high-strength steel tubular sections, J. Struct. Eng. 142 (2016) 04015174.
[63] RUOSTE, Rules on High Strength Steel, European Commission, 2015.
[64] L. Gao, H. Sun, F. Jin, H. Fan, Load-carrying capacity of high-strength steel box-sections I: Stub columns, J. Constr. Steel Res. 65 (2009) 918–924.
[65] SEMI-COMP, Plastic Member Capacity of Semi-Compact Steel Sections – A more Economic Design, European Commission, 2009.
[66] Y.J. Guo, A.Z. Zhu, Y.L. Pi, F. Tin-Loi, Experimental study on compressive strengths of thick-walled cold-formed sections, J. Constr. Steel Res. 63 (2007) 718–723.
[67] K. Sakino, H. Nakahara, S. Morino, I. Nishiyama, Behavior of centrally loaded concrete-filled steel-tube short columns, J. Struct. Eng. 130 (2004) 180–188.
[68] M. Elchalakani, X.L. Zhao, R. Grzebieta, Tests on concrete filled double-skin (CHS outer and SHS inner) composite short columns under axial compression, Thin-Walled Struct. 40 (2002) 415–441.
[69] R.M. Sully, G.J. Hancock, Behavior of cold-formed SHS beam-columns, J. Struct. Eng. 122 (1996) 326–336.
[70] P.W. Key, S.W. Hasan, G.J. Hancock, Column behavior of cold-formed hollow sections, J. Struct. Eng. 114 (1988) 390–407.
[71] S.D. Hu, B. Ye, L.X. Li, Materials properties of thick-wall cold-rolled welded tube with a rectangular or square hollow section, Constr. Build Mater. 25 (2011) 2683–2689.
[72] K. Washio, N. Ishihama, Local instability of lipped chanel and rectangular-tube sections and their equivalent widths (part I) (in Japanese), Trans. Archit. Inst. Jpn. 139 (1967) 33–43, 78.
[73] T.G. Singh, K.D. Singh, Structural performance of YSt–310 cold–formed tubular steel stub columns, Thin-Walled Struct. 121 (2017) 25–40.
[74] M. Kettler, Elastic-Plastic Cross-Sectional Resistance of Semi-Compact H- and Hollow Sections (Ph.D. thesis), Graz University of Technology, 2008.
[75] R.J. McDermott, Column Strength of Cold-Formed Tubular Sections (MS thesis), Lehigh University, 1981.
[76] prEN 1993-1-5:2022, Eurocode 3. Design of Steel Structures. Part 1-5. Plated Structural Elements, European Committee for Standardization (CEN), 2022.
[77] A. Liew, L. Gardner, Ultimate capacity of structural steel cross-sections under compression, bending and combined loading, Structures 1 (2015) 2–11.
[78] L. Gardner, X. Yun, F. Walport, The continuous strength method – Review and outlook, Eng. Struct. 275 (2023) 114924.